

A blast from the infant Universe: the very high- z GRB 210905A \star

A. Rossi^{1, **}, D. D. Frederiks², D. A. Kann³, M. De Pasquale⁴, E. Pian¹, P. D'Avanzo⁵, L. Izzo⁶, G. Lamb⁷, D. B. Malesani^{8, 9, 10}, A. Melandri⁵, A. Nicuesa Guelbenzu¹¹, S. Schulze¹², R. Strausbaugh¹³, L. Amati¹, S. Campana⁵, A. Cucchiara^{13, 14}, G. Ghirlanda^{5, 15}, M. Della Valle¹⁶, S. Klose¹¹, R. Salvaterra¹⁷, R. Starling¹⁸, G. Stratta¹, N. R. Tanvir¹⁸, A. E. Tsvetkova², S. D. Vergani^{5, 19, 20}, A. D'Ai²¹, D. Burgarella²², S. Covino⁵, V. D'Elia^{23, 24}, A. de Ugarte Postigo²⁵, H. Faussey²⁶, J. P. U. Fynbo^{9, 10}, F. Frontera^{1, 27}, C. Guidorzi^{1, 27, 28}, K. E. Heintz^{9, 29}, A. J. Levan⁸, N. Masetti^{1, 30}, E. Maiorano¹, C.G. Mundell³¹, S. R. Oates³², M. J. Page³³, E. Palazzi¹, J. Palmerio¹⁹, G. Pugliese^{34, 35}, A. Rau³⁶, A. Saccardi¹⁹, B. Sbarufatti^{5, 37}, D. S. Svinkin², G. Tagliaferri⁵, A. J. van der Horst^{26, 38}, D. Watson⁶, M. V. Ulanov², K. Wiersema³⁹, D. Xu^{40, 41}, and J. Zhang (张洁莱)^{42, 43}

(Affiliations can be found after the references)

Received xx, xx; accepted xx, xx

ABSTRACT

We present the discovery of the very energetic GRB 210905A at the high redshift $z = 6.312$ and its luminous X-ray and optical afterglow. Following the detection by *Swift* and *Konus-Wind*, we obtained photometric and spectroscopic follow-up in the optical and near-infrared (NIR), covering both the prompt and afterglow emission from a few minutes up to 7.5 Ms after burst. With an isotropic gamma-ray energy of $E_{\text{iso}} = 1.27_{-0.19}^{+0.20} \times 10^{54}$ erg, GRB 210905A lies in the top $\sim 7\%$ GRBs in the *Konus-Wind* Catalog in terms of energy released. Its afterglow is among the most luminous ever observed, and, in particular, it is one of the most luminous in the optical at $t \gtrsim 0.5$ d, in the rest frame. The afterglow starts with a shallow evolution that can be explained by energy injection, and is followed by a steeper decay, while the spectral energy distribution is in agreement with slow cooling in a constant-density environment within the standard fireball theory. A jet break at $\sim 39 \pm 21$ d has been observed in the X-ray light curve; however, it is hidden in the *H* band, potentially due to a constant contribution from an unknown component, most likely a foreground intervening galaxy and/or the host galaxy. We derived a half-opening angle of $7.9^\circ \pm 1.6^\circ$, the highest ever measured for a $z \gtrsim 6$ burst but within the range covered by closer events. The resulting collimation-corrected released gamma-ray energy of $\simeq 1 \times 10^{52}$ erg is also among the highest ever measured. The moderately large half-opening angle argues against recent claims of an inverse dependence of the half-opening angle on the redshift. The total jet energy is likely too large to be sustained by a standard magnetar, and suggests that the central engine of this burst was a newly formed black hole. Despite the outstanding energetics and luminosity of both GRB 210905A and its afterglow, we demonstrate that they are consistent within 2σ with those of less distant bursts, indicating that the powering mechanisms and progenitors do not evolve significantly with redshift.

Key words. gamma-ray burst: general – Gamma-ray burst: individual: GRB 210905A

1. Introduction

The discovery of a $z > 6$ gamma-ray burst (GRB) is a rare occurrence that, thanks to the extreme luminosity of these sources, offers a window into an infant Universe, which is otherwise difficult to observe. Long GRBs, with gamma-ray emission episodes generally longer than 2 s (Kouveliotou et al. 1993), originate from the explosions of very massive stars (Hjorth et al. 2003; Stanek et al. 2003; Woosley & Bloom 2006). Under the assumptions that the stellar Initial Mass Function (IMF) in distant galaxies is not broadly different from that of closer objects and that the opening angles do not evolve strongly with redshift, the rate of GRBs can be used both to estimate the star-formation rate (SFR) (Kistler et al. 2009; Robertson & Ellis 2012) and to study the effects of metallicity on the SNe-Ibc and GRB progenitors (Grieco et al. 2012). The SFR is expected to change at very high redshift with the transition from the first massive Population III (Pop-III) stars in the remote Universe to Pop-II/I stars (Salvaterra 2015; Fryer et al. 2021). How this happens remains

\star Based on observations collected at the Very Large Telescope of the European Southern Observatory, Paranal, Chile (ESO program 106.21T6; PI: N. Tanvir), REM (AOT43; program 43008; PI: A. Melandri), and GROND (0106.A-9099(A); PI: A. Rau).

** E-mail: andrea.rossi@inaf.it

an open question that may be addressed through GRB studies. Note that the prompt emission is not affected by dust extinction, and thus GRBs can provide a census of obscured star-formation at all redshifts (Blain & Natarajan 2000). Due to their immense brightness, GRBs can also act as beacons illuminating the local circumburst medium (e.g., Prochaska et al. 2008; Schady et al. 2011; Watson et al. 2013; Heintz et al. 2018), the Inter-Stellar Medium (ISM) of their hosts (e.g., Fynbo et al. 2006; Cucchiara et al. 2015; Bolmer et al. 2019; Heintz et al. 2019), and the surrounding InterGalactic Medium (IGM) in the line of sight (Totani et al. 2006; Hartoog et al. 2015). They are therefore powerful probes of the ionization and chemical enrichment history of the early universe. To shed light on these open issues through very high-redshift GRBs, several mission concepts have been studied and proposed (e.g., Amati et al. 2018; Tanvir et al. 2021b; White et al. 2021).

So far, out of the ≈ 550 GRBs with a well-constrained spectroscopic redshift (as of 31 January 2022), only five have been detected¹ at $z \gtrsim 6$: GRB 050904 ($z = 6.295$, Kawai et al. 2006; Tagliaferri et al. 2005a), GRB 080913 ($z = 6.733$, Greiner et al. 2009; Patel et al. 2010), GRB 090423A ($z = 8.23$, Tanvir et al. 2009; Salvaterra et al. 2009), GRB 130606A ($z = 5.913$, Har-

¹ See <http://www.mpe.mpg.de/~jcg/grbgen.html>

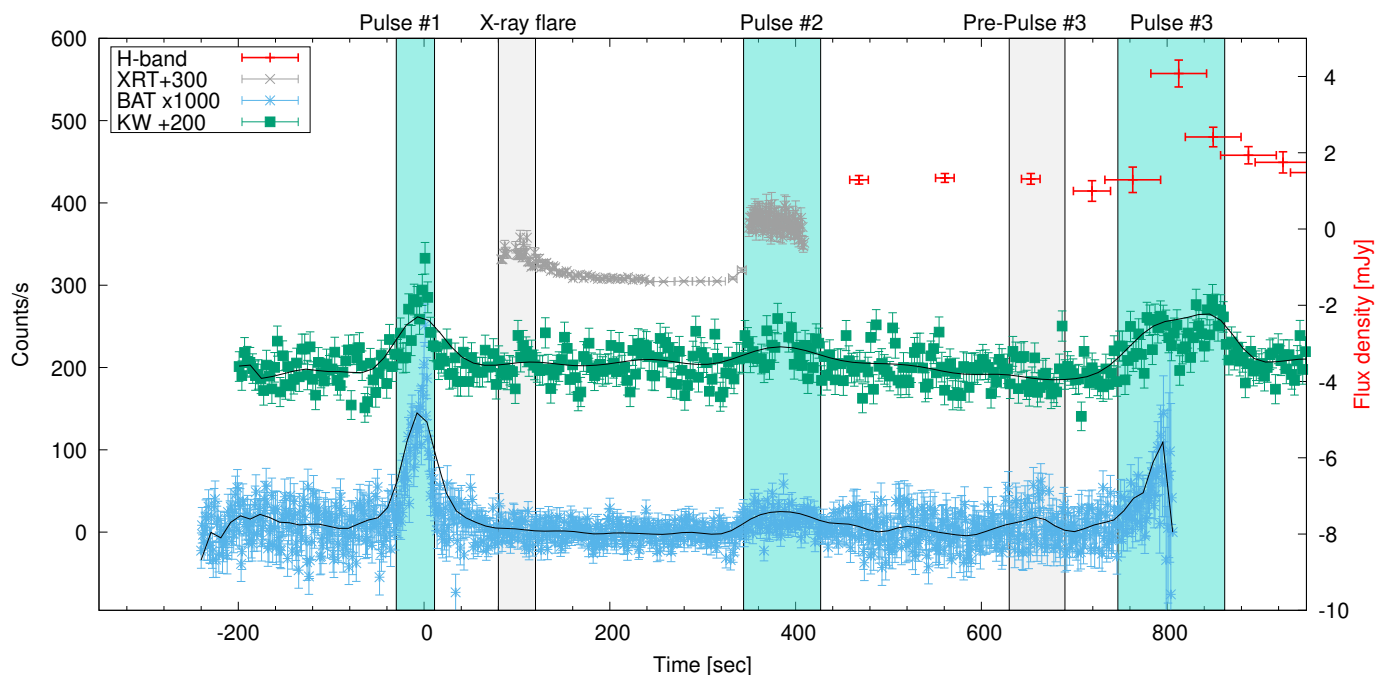


Fig. 1. Multi-band prompt emission light curve of GRB 210905A. The light curve of GRB 210905A as seen by *Swift*/BAT (15 – 350 keV, 6 s binning, counts \times 1000, cyan), *Konus-Wind* (20 – 400 keV, 5.888 s binning, counts + 200, green points), *Swift*/XRT (counts + 300, grey points) and REM (Flux density, red points). The evolution of the gamma-ray emission is highlighted with a black smoothed spline to guide the eye. The intervals corresponding to the three pulses and the intermediate epochs are highlighted by turquoise and grey-shaded areas, respectively.

toog et al. 2015; Chornock et al. 2013)², and GRB 140515A ($z = 6.327$, Chornock et al. 2014; Melandri et al. 2015). An additional four have very low signal-to-noise spectra or photometric redshifts: GRB 090429B ($z \approx 9.4$, Cucchiara et al. 2011), GRB 100905A ($z \approx 7.88$, Bolmer et al. 2018), GRB 120521C ($z \approx 6$, Laskar et al. 2014), and GRB 120923A ($z \approx 7.8$, Tanvir et al. 2018). Some of these events show larger prompt energetics than those at low redshift, but this is likely the result of observational biases, and a cosmic evolution of the GRB energy release function is not confirmed yet (e.g., Tsvetkova et al. 2017, 2021, and references therein). In fact, also very-high redshift GRBs follow the ($E_{\text{peak},z} - E_{\text{iso}}$ and $E_{\text{peak},z} - L_{\text{iso}}$ correlations (Amati/Yonetoku correlations; Amati et al. 2002; Yonetoku et al. 2004). The same is true for the afterglow luminosity (Kann et al., 2022a, in prep.), which is larger only when compared with the low-luminosity and really nearby events ($z < 0.2$). The large prompt energy release is well-matched by a larger X-ray luminosity of their afterglows, as indeed the L_X/E_{iso} is similar to that of low-redshift events. These results suggest that the powering mechanisms and progenitors do not evolve with redshift. On the other hand, some studies have suggested that jets from GRBs in the high-redshift universe are more narrowly collimated than those at lower redshifts (e.g., Lloyd-Ronning et al. 2019; Laskar et al. 2014, 2018) which would imply that more stars formed at high redshift than previously estimated (Lloyd-Ronning et al. 2020a).

Here we present the discovery of the bright GRB 210905A, the tenth burst with redshift $z \gtrsim 6$ detected in the last 16 years. It was detected by the *Neil Gehrels Swift Observatory* (Gehrels et al. 2004, *Swift* hereafter) and *Konus-Wind* (Aptekar et al. 1995). X-ray and optical/near-infrared (NIR) follow-up observations of its bright afterglow led us to determine a spectro-

scopic redshift of $z = 6.312$ (refined with respect to Tanvir et al. 2021a). The burst was also detected by the Cadmium Zinc Telluride Imager (CZTI) on-board *Astrosat* (Prasad et al. 2021) and, following the detection by the *Swift* Burst Alert Telescope (BAT, Barthelmy et al. 2005a), was found via targeted search in data of the Gamma-ray Burst Monitor (GBM) on-board *Fermi* (Veres et al. 2021).

In §2 we describe the observations of both the GRB and the afterglow, and in §3 we present the analysis of the data. In §4 we discuss the results and compare with other bursts at low and high redshift, and we conclude in §5. Throughout this work, the flux density of the afterglow is described as $F_\nu(t) \propto t^{-\alpha} \nu^{-\beta}$. A Λ CDM cosmological model with $\Omega_M = 0.308$, $\Omega_\Lambda = 0.692$, and $H_0 = 67.8 \text{ km s}^{-1} \text{ Mpc}^{-1}$ (Planck Collaboration et al. 2016) has been assumed for calculations. All data are in observer frame and 1σ errors are used throughout the paper, unless differently specified.

2. Observations

2.1. Gamma-ray and X-ray observations.

GRB 210905A was discovered by BAT on-board *Swift* at $T_0 = 00:12:41.3$ UT on 5 September 2021 (Sonbas et al. 2021). The BAT light curve shows a complex structure with three pulses, detected until ~ 800 s after the burst trigger.

Since GRB 210905A was too weak to trigger³ *Konus-Wind* (KW), the burst data are available only from the instrument’s waiting mode, as first reported by Frederiks et al. (2021). In this mode, count rates with a coarse time resolution of 2.944 s are recorded continuously in three energy bands: G1 (20 – 100 keV),

² We consider this burst to be at $z \sim 6$, as it lies just below this threshold.

³ See §4.3 of Tsvetkova et al. (2021) for details on the KW trigger sensitivity.

G2 (100 – 400 keV), and G3 (400 – 1500 keV). A Bayesian block analysis of the KW waiting mode data in S1 (one of the two NaI(Tl) detectors) reveals three (separated in time) emission episodes, each featuring a statistically significant count rate increase in the combined G1+G2 band (Fig. 1), while no statistically significant emission was detected in the G3 band throughout the burst.

The first episode, which triggered *Swift*/BAT, started at $\approx T_0 - 30$ s and ends at $\approx T_0 + 11$ s (hereafter Pulse 1). The weaker second episode ($\sim T_0 + 344$ s to $\sim T_0 + 426$ s; Pulse 2) coincided in time with the bright flare in the XRT windowed-timing (WT) mode light curve around $T_0 + 400$ s (Fig. 1). The onset of the final emission episode, observed by KW from $\sim T_0 + 747$ s to $\sim T_0 + 862$ s (Pulse 3), is clearly visible in the BAT mask-weighted data, which are available up to ~ 800 s after the trigger. The T_{90} duration⁴ of the GRB 210905A prompt emission derived from the KW observation is ~ 870 s.

Swift/XRT started to observe the BAT error circle 91.7 s after the trigger and found an unknown X-ray source at the enhanced position of coordinates RA (J2000) = $20^{\text{h}}36^{\text{m}}11^{\text{s}}.64$, Dec. (J2000) = $-44^{\circ}26'24''.3$ with a final uncertainty of $1''.5$ (Beardmore et al. 2021, *Swift*/XRT catalogue). Pointed *Swift* observations continued until 3.8 Ms after the GRB, when the source became too faint to be detected. Light curves and spectra, as well as the result of their modelling, have been obtained from the *Swift*/XRT repository (Evans et al. 2007, 2009). However, to build more accurate multi-wavelength spectral energy distributions (SEDs), given that some data available in the *Swift*/XRT repository suffer from bad centroid determination, we have processed the *Swift* data corresponding to the epochs of our SED analysis (Obs. ID 01071993001/002/003), Fig. 4. To reduce the data, the software package HeaSoft 6.29 was used⁵ with the latest calibration file available⁶. For the data processing, we used standard procedures, consisting of the use of the package xrtpipeline, available within the FTOOLS distribution⁷, with standard-grade filtering. Using the most refined position provided by the *Swift* team, the selection of the GRB position in the X-ray data, and the following extraction of source and background spectra, was done with the xselect package, while for the construction of the corresponding ancillary response file (.arf) we used xrtmkarf on each corresponding epoch exposure file.

In the following, a Galactic equivalent hydrogen column density of $N_H = 3.38 \times 10^{20} \text{ cm}^{-2}$ is adopted (Willingale et al. 2013).

2.2. Optical/NIR imaging and photometry

Swift/UVOT started observing about 156 s after the trigger but no credible afterglow candidate was found (Siegel et al. 2021). The MASTER Global Robotic Net (Lipunov et al. 2010) was also pointed at GRB 210905A 6 s after notice time and 414 s after trigger time but could not detect any afterglow candidate (Lipunov et al. 2021).

We obtained optical/NIR observations with the 0.6m robotic Rapid Eye Mount telescope (REM, Zerbi et al. 2001), starting 428 s after the burst. A transient source was detected immediately in the H band and later in $i'z'ZJK$ bands (i.e., all except g'

Table 1. Optical/NIR photometry of the afterglow (AB magnitudes).

Δt^a (days)	Magnitude AB ^b	Filter	Telescope
0.11410	> 25.0	g'	VLT/XS
0.10930	> 24.8	r'	VLT/XS
0.03771	> 22.5	R_C	LCO
0.05867	19.46 ± 0.14	I_C	LCO
0.10739	20.35 ± 0.14	I_C	LCO
0.13519	20.41 ± 0.15	I_C	LCO
0.10627	20.52 ± 0.06	I_{Bessel}	VLT/XS
87.0326 ^c	26.15 ± 0.40	I_{Bessel}	VLT/FORS2
0.02651	20.86 ± 0.46	i'	REM
0.19712	22.78 ± 0.03	i'	Blanco/DECam
0.02614	18.17 ± 0.33	Z	REM
0.03065	18.23 ± 0.37	z'	REM
0.05048	18.48 ± 0.29	Z	REM
0.07097	> 18.1	z'	REM
0.10722	19.20 ± 0.40	Z	REM
0.11129	19.53 ± 0.02	z'	VLT/XS
0.98756	21.61 ± 0.12	z'	MPG/GROND
2.09740	22.34 ± 0.18	z'	MPG/GROND
0.01489	17.12 ± 0.15	J	REM
0.02402	17.52 ± 0.16	J	REM
0.03315	17.45 ± 0.19	J	REM
0.04662	17.81 ± 0.15	J	REM
0.11155	18.86 ± 0.22	J	REM
0.98756	20.26 ± 0.11	J	MPG/GROND
2.09740	21.14 ± 0.12	J	MPG/GROND
0.00542	16.15 ± 0.09	H	REM
0.00649	16.11 ± 0.09	H	REM
0.00756	16.13 ± 0.11	H	REM
0.00832	16.43 ± 0.26	H	REM
0.00883	16.15 ± 0.25	H	REM
0.00940	14.90 ± 0.09	H	REM
0.00983	15.47 ± 0.11	H	REM
0.01027	15.71 ± 0.12	H	REM
0.01070	15.82 ± 0.16	H	REM
0.01114	16.00 ± 0.13	H	REM
0.02397	17.32 ± 0.12	H	REM
0.03853	17.55 ± 0.16	H	REM
0.09519	18.35 ± 0.21	H	REM
0.98756	20.08 ± 0.12	H	MPG/GROND
0.98777	20.08 ± 0.06	H	VLT/HAWK-I
2.07128	20.78 ± 0.06	H	VLT/HAWK-I
2.0974	20.64 ± 0.14	H	MPG/GROND
3.97651	21.49 ± 0.06	H	VLT/HAWK-I
10.9949	22.61 ± 0.11	H	VLT/HAWK-I
27.0106	23.23 ± 0.14	H	VLT/HAWK-I
52.0603	24.03 ± 0.14	H	VLT/HAWK-I
0.01259	16.16 ± 0.15	K	REM
0.02172	16.72 ± 0.24	K	REM
0.03085	17.07 ± 0.28	K	REM
0.04257	17.14 ± 0.23	K	REM
0.10746	18.33 ± 0.38	K	REM
0.98756	20.17 ± 0.20	K_s	MPG/GROND
1.00021	19.89 ± 0.03	K_s	VLT/HAWK-I

^a Mid-time after the *burst* trigger.

^b The photometry is not corrected for Galactic extinction.

^c Possible foreground source.

and r'). Observations continued for about three hours before the declining afterglow brightness fell below the instrument detection limits in all filters (D'Avanzo et al. 2021). Images were automatically reduced using the jitter script of the eclipse package (Devillard 1997) which aligns and stacks the images to obtain

⁴ The total duration (T_{100}) derived from the KW observation is ~ 890 s (at the 5σ level).

⁵ <http://heasarc.gsfc.nasa.gov/docs/software/lheasoft>

⁶ *Swift*/XRT Calibration Files: 20210915

⁷ <http://heasarc.gsfc.nasa.gov/ftools/>

one average image for each sequence. A combination of IRAF (Tody 1993) and SExtractor packages (Bertin & Arnouts 2010) were then used to perform aperture photometry.

We triggered Bessel R - and I -band observations with the 1m telescope of the Las Cumbres Observatory Global Telescope (LCOGT) network, equipped with the Sinistro instrument, at the Cerro Tololo Inter-American Observatory (CTIO), Chile. The midpoints of the first epoch are $t_I = 1.06$ and $t_R = 1.29$ hours, in I and R bands respectively. The data provided by the LCO are reduced using the BANZAI pipeline (McCully et al. 2018) that performs bias and dark subtraction, flat-fielding, bad-pixel masking, and astrometric calibration. Afterwards, we use our own pipeline, which aligns and stacks the images using the astroalign Python package (Beroiz et al. 2020), and afterwards uses SExtractor to perform the photometry and calibration against a sample of USNO-B catalog stars (Monet et al. 2003). Using the data-reduction pipeline from LCO, and our relative photometry pipeline⁸, we calculate a magnitude of $I = 19.46 \pm 0.15$ mag and a 3σ upper limit of $R > 22.44$ mag. The lack of an R -band detection alerted us to the possibility that this burst may lie at very high redshift ($z > 5$) (first reported in Strausbaugh & Cucchiara 2021b,a).

GRB 210905A was observed simultaneously in $g'r'i'z'JHK$ with GROND (Gamma-Ray Burst Optical Near-Infrared Detector; Greiner et al. 2008; Greiner 2019) mounted on the 2.2m MPG telescope at ESO La Silla Observatory in Chile (Nicuesa Guelbenzu et al. 2021). The first epoch observations were done around 23 hours after the GRB trigger. The afterglow was detected only in the $z'JHK$ bands. A second set of observations obtained seven hours later was shallower and yielded only upper limits. Subsequent follow-up observations were obtained on 7 and 8 September 2021, but the afterglow was also not detected in the latter epoch. We continued our ground-based follow-up using both the VLT/HAWK-I NIR imager on Paranal (High Acuity Widefield K-band Imager, Pirard et al. 2004), as well as the Dark Energy Camera (DECam) mounted on the 4m Victor Blanco telescope at CTIO. We also used the acquisition camera of the ESO VLT/X-shooter spectrograph to obtain $g'r'I_{Bessel}z'$ imaging before moving on to spectroscopy. We obtained a last observation 87 d after the GRB with VLT/FORS2 in the I_{Bessel} band.

X-shooter and GROND optical/NIR images were reduced in a standard manner using PyRAF/IRAF (Tody 1993). In particular, GROND data reduction was done with a customized pipeline (Krühler et al. 2008) that is based on standard routines in IRAF. FORS I -band and HAWK-I JHK_s -band data have been reduced using the ESO Reflex environment (Freudling et al. 2013). We obtained PSF photometry with the DAOPHOT and ALLSTAR tasks of IRAF. PSF-fitting was used to measure the magnitudes of the GRB afterglow.

All optical photometry except I_{Bessel} -band data were calibrated against the SkyMapper catalog (Wolf et al. 2018), while the NIR photometric calibration was performed against the 2MASS catalog (Skrutskie et al. 2006). This procedure results in a typical systematic accuracy of 0.04 mag in $g'r'i'z'$, 0.06 mag in JH and 0.08 mag in K_s . To cross-calibrate all the I -band imaging we applied the Lupton formulae to a set of local standard stars from the SkyMapper catalog.

The I filters used by X-shooter and LCO extend beyond 10000 Å. Therefore, we expect that not all the flux is dimmed by the Lyman- α dropout at ~ 8900 Å in these filters. On the contrary, the FORS2 I -band filter has negligible transmission above

Lyman- α (at the redshift of GRB 210905A). Therefore, we speculate that the possible (note the large error) late I -band emission reported in Table 1 does not originate from the afterglow, but instead from a foreground source (see § 3.5).

The optical/NIR afterglow lies at coordinates RA (J2000) = $20^h36^m11^s57$, Dec. (J2000) = $-44^\circ26'24''.7$ as measured in our HAWK-I images and calibrated against field stars in the GAIA DR2 catalogue (Gaia Collaboration et al. 2018) with the astrometric precision being $0''.15$. This refines the position reported by LCO (Strausbaugh & Cucchiara 2021b) and is in agreement with the more precise localization provided by ALMA (Laskar et al. 2021a). Table 1 provides a summary of all photometry of the transient (non-relevant upper limits are not reported). All reported magnitudes are in the AB photometric system and not corrected for the Galactic foreground extinction of $E(B-V) = 0.029$ mag (Schlafly & Finkbeiner 2011).

2.3. X-shooter spectroscopy and redshift

Starting ~ 2.53 hours after the GRB detection, we obtained UV to NIR spectroscopy of the afterglow with the X-shooter instrument (Vernet et al. 2011) mounted on the VLT on Cerro Paranal (ESO, Chile), via the STARGATE Large Programme for GRB studies.

The afterglow is well-detected in the red part of the visible arm. A clear break is detected around 9000 Å, which we interpret as the Lyman- α break (first reported in Tanvir et al. 2021a). Other lines such as Fe II, Al II, C IV and Si II and fine structure lines are visible and display two velocity components, which belong to the ISM of the same galaxy. All these lines allow us to determine $z = 6.312$ as the redshift of the GRB. The details concerning the reduction and analysis of the absorption lines in the X-shooter spectra is given in Saccardi et al. (in prep.). This high redshift explains the non-detection by UVOT and MASTER and confirms the red $R_C - I_C$ and $r' - z'$ colors found with LCO and X-shooter as due to Lyman dropout. In Fausey et al. (in prep.) we will study the IGM neutral fraction in light of the GRB 210905A afterglow spectrum.

3. Modelling and results

3.1. Joint BAT-KW modelling

To derive the broad-band spectral parameters of the prompt emission of this burst, we performed a joint spectral analysis of the BAT data (15 – 150 keV) and the KW waiting-mode data (20 – 1500 keV) for all three prompt emission episodes in a way similar to that described in Tsvetkova et al. (2021).

The spectral data from the two instruments were simultaneously fit in Xspec v12.12.0 using three different spectral models (see below), all normalized to the energy flux in the 15 – 1500 keV range. The most reliable results for all three emission episodes were obtained with a power-law function with high-energy exponential cutoff (CPL). Compared to the CPL, a simple power-law (PL) function fits the data with significantly worse statistics ($\Delta\chi^2 > 7$ in all cases) and systematically overestimates the high-energy part of the spectra. The Band function (Band et al. 1993) does not improve the fit statistics as compared to the CPL. For all spectra, the Band fits⁹ provide values of the index α and E_{peak} almost identical to the CPL fits (and consistent within the large errors), and set only an upper limit on the

⁸ The photometry was confirmed after the cross-calibration mentioned below.

⁹ The Band function has parameters α , β and E_{peak} , not to be confused with the decay and spectral indexes of the afterglow, defined in §1.

Table 2. Fits to the prompt emission spectra.

Spectrum ^a	Instruments	Model ^f	Time interval (relative to T_0 , s)	α (PL index)	E_{peak} or ν_m (keV)	E_{break} or ν_c (keV)	Flux (15–1500 keV) (10^{-7} erg cm $^{-2}$ s $^{-1}$)	χ^2 (d.o.f.)
'peak' ^b	BAT+KW	CPL	[−0.465, 2.479]	$-0.66^{+0.35}_{-0.30}$	144^{+56}_{-28}		$2.83^{+0.56}_{-0.40}$	40.2 (58)
Pulse 1	BAT+KW	CPL	[−29.905, 11.311]	$-0.99^{+0.18}_{-0.17}$	127^{+31}_{-19}		$1.14^{+0.14}_{-0.11}$	36.5 (58)
Pulse 1	"	DBPL	"		127	$27.09^{+3.41}_{-3.34}$		35.2 (56)
X-ray flare ^c	XRT+KW	DBPL	[80.0, 120.0]		$1.46^{+0.21}_{-0.26}$	unconstrained		225.9 (281)
Pulse 2	XRT+BAT+KW	CPL	[343.983, 426.415]	$-0.80^{+0.58}_{-0.47}$	70^{+22}_{-13}		$0.28^{+0.06}_{-0.05}$	48.6 (58)
Pulse 2	"	DBPL	"		50	$1.13^{+0.11}_{-0.10}$		714.2 (714)
Pulse 3 ^d	BAT	CPL	[747.311, 797.359]	$-0.89^{+0.37}_{-0.30}$	154^{+77}_{-36}		$0.76^{+0.17}_{-0.11}$	55.2 (58)
Pulse 3 ^e	KW	CPL	[747.311, 862.127]	$-0.88^{+0.76}_{-0.30}$	167^{+88}_{-61}		$0.97^{+0.24}_{-0.23}$	0 (0) ^e
Pulse 3 ^e	REM+BAT+KW	DBPL	[747.311, 797.359]		154	0.006 ^g		59.3 (56)

^a All spectra, except the first, are time-averaged.

^b This spectrum was used to calculate the peak energy flux.

^c The interval covered by XRT.

^d The interval covered by BAT.

^e KW-only fit; for the CPL model, the 3-channel fit has 0 degrees of freedom.

^f CPL stands for cut-off power-law. DBPL stands for double-broken power-law, used for the synchrotron model. In this last case, the power-law indexes were fixed as described in §3.2.

^g This break was fixed to match the H -band data.

high-energy photon index ($\beta < -2.3$), due to the sparse KW data which do not provide enough sensitivity and spectral resolution to constrain the spectral index above 100 keV.

Our fits with the CPL function are summarized in Table 2. The time-averaged spectrum of the brightest episode (Pulse 1) is best described by $\alpha \sim -0.99$ and observed $E_{\text{peak}} \sim 127$ keV. The spectrum of the weaker episode (Pulse 2) is characterized by a similar, within errors, α , and an about halved $E_{\text{peak}} \sim 70$ keV. The third emission episode is ~ 115 s long and only partially covered by *Swift*/BAT. In this case, we analyzed the spectra extracted for two time intervals: the first spectrum corresponds to the time interval of joint KW and BAT detection ($\alpha \sim -0.89$, $E_{\text{peak}} \sim 154$ keV), and the second one covers the whole third emission episode ($\alpha \sim -0.88$, $E_{\text{peak}} \sim 167$ keV). For the latter interval, the fits were made using the KW 3-channel spectrum alone and the obtained model flux was used to calculate the Pulse 3 energy fluence.

The 15 – 1500 keV energy fluences of Pulses 1, 2, and 3, derived from our time-averaged fits, are summarized in Table 5, together with the fluence integrated over all three emission episodes. We use these results to calculate the isotropic energy (see also §4.2). The spectrum in the interval ($T_0 - 0.465$, $T_0 + 2.479$) inside Pulse 1, which corresponds to the peak count rate, is characterized by $\alpha \sim -0.66$ and $E_{\text{peak}} \sim 144$ keV. Using this spectrum and the BAT light curve, we estimate the 1 s peak energy flux of GRB 210905A to be $3.83^{+0.73}_{-0.54} \times 10^{-7}$ erg cm $^{-2}$ s $^{-1}$ (15 – 1500 keV).

3.2. Joint modelling of the prompt emission from gamma-rays to the optical

In the previous section we have analyzed the gamma-ray spectra during the three pulses and found that they can be modelled almost equally well with a CPL or a Band function with very similar (within errors) low-energy photon index $\sim -0.8 <$

$\alpha < -1.2$ and E_{peak} . The high-energy index of the Band function is $\beta < -2.3$, poorly constrained by the sparse KW data. Values of -1 and -2.3 are very typical low- and high-energy photon indices for GRBs (e.g., Preece et al. 1998; Nava et al. 2011). Following early works (Frontera et al. 2000; Rossi et al. 2011; Zheng et al. 2012), recently Oganesyanyan et al. (2019) have shown that the low-energy spectra (< 100 keV) of the majority of *Swift*/BAT GRBs actually have a low-energy spectral break at $\sim 2 - 30$ keV, in addition to the typical break corresponding to the peak energy at larger energies. Such a break has also been discovered at higher energies, up to few hundreds of keV, in *Fermi* bursts (Ravasio et al. 2018, 2019) and has been suggested to be a common feature of GRB prompt emission spectra (Toffano et al. 2021). Therefore, the low-energy photon index -1 can be broken into two power-law photon indices describing the spectrum below and above the low-energy break, and have distributions centred around $-2/3$ and $-3/2$ (or $1/3$ and $-1/2$ for an energy spectrum F_ν), respectively. These indices are the same as those below and above the cooling break ν_c and expected by the synchrotron theory in the fast-cooling regime (see also Ravasio et al. 2018, 2019). Further confirmation of these empirical fits was obtained by direct fitting of prompt GRB spectra with a synchrotron model (Ronchi et al. 2020; Burgess et al. 2020) and the synchrotron interpretation is discussed in, e.g., Ghisellini et al. (2020).

To determine if the prompt emission of GRB 210905A is in agreement with these theoretical expectations, we have modelled the NIR and X- to gamma-ray SEDs of five epochs during the whole prompt emission with a double broken power-law with photon indices fixed to the synchrotron model. That the optical-to-gamma emission is the result of a common radiative process is justified by the simultaneous evolution of the optical, X-ray and gamma-ray prompt emission. The selected epochs are the three gamma-ray pulses, the first X-ray flare at ~ 120 s and an additional epoch at $\sim 630 - 690$ s simultaneous to an H -

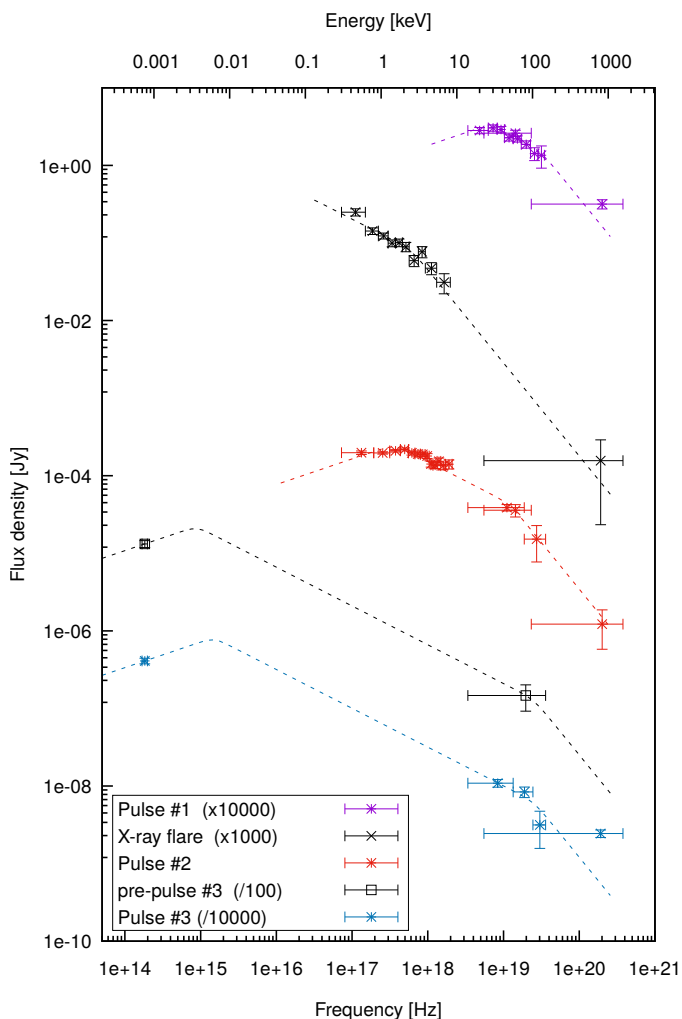


Fig. 2. Optical/NIR to gamma-ray SEDs of the prompt phase at five different epochs (see § 3.2). All SEDs have been modelled with a double broken power-law following the expectations from synchrotron theory. Note that we could not constrain the low-energy break during the X-ray flare. In the fourth SED, we have simply scaled the solution from the last epoch (there is no KW detection during this epoch). Note that the photon indices described in the text correspond to spectral indices $1/3$, $-1/2$, -1.3 shown here. X-ray data are corrected for Galactic and intrinsic absorption.

band observation. This is the only epoch before the last pulse with few counts in the BAT spectrum. We have fixed the high-energy break (ν_m , the minimum injection energy in a fast-cooling synchrotron model) to the break energy in the Band modelling above. The high-energy photon index above this break has been fixed to -2.4 , i.e., also consistent with the Band fit. The results are shown in Table 2 and in Fig. 2. The analysis of the X-ray flare alone shows that it is well modelled by ν_m at ~ 1 keV, a photon index¹⁰ -2.4 and intrinsic absorption $N_H = 7.7^{+3.6}_{-3.2} \times 10^{22}$ cm $^{-2}$. In the following, we fixed the intrinsic hydrogen column density to this value. During the first two pulses the data are consistent with a broken power-law with photon index 0.5.

In the last two SEDs, we also include the H -band follow-up obtained with REM (Fig. 1). Note that in the fourth SED we have simply scaled the solution from the last epoch, because there are basically just two measurements for three possible free param-

¹⁰ We could not constrain the low-energy break for this epoch.

Table 3. Optical/NIR to X-ray modelling of the afterglow (see Fig. 4).

Model	Time d	β_{opt}^a	Break (keV)		χ^2 / d.o.f.
			obs.	Theor. ^b	
BPL	0.1	0.62 ± 0.04	$1.7^{2.6}_{-1.6}$	1.4 ± 1.2	9.8/16
SPL	0.1	0.63 ± 0.03	–	–	9.9/17
BPL	1.0	0.60 ± 0.04	$0.35^{0.28}_{-0.13}$	0.35	63.1/53
SPL	1.0	0.71 ± 0.02	–	–	75.8/54
BPL	2.2	0.56 ± 0.16	$0.18^{0.06}_{-0.03}$	0.22 ± 0.19	22.8/25
SPL	2.2	0.80 ± 0.03	–	–	19.5/26

^a In the broken power-law we assumed $\beta_X = \beta_{opt} + 0.5$.

^b Obtained from the best-fit value at 1 d with $\nu(t) = \nu(1d)(t/1d)^{-k}$, with $k = 0.5$ after 1 d (ISM, slow cooling scenario) and $k = 0.6$ before 1 d assuming energy injection (see § 4.4).

ters¹¹, not enough to constrain all breaks. Therefore, this is not shown in Table 2.

For these last SEDs (i.e., before and during the Pulse 3) the H -band observation is below the extrapolation of the photon index from the gamma-rays, and thus ν_c must be in between the H and X-ray bands. We further discuss the implications of this finding in § 4.1. Unfortunately, for both SEDs the lack of any color information and possible contribution from the emerging afterglow in the observed optical/NIR prevents us to affirm without doubt that the low-energy photon index is $-2/3$. However, we can confirm that for both SEDs the synchrotron model is in agreement with the observations.

3.3. Joint afterglow light curve and SED

Fig. 3 shows both optical/NIR and X-rays light curves of the afterglow. Regions in grey have not been considered in this section because of: i) the presence of flares due to the prompt emission and ii) a possible late break when compared to the earlier evolution (Fig. 3) that we discuss below in § 3.4.

A complete understanding of the afterglow behavior would require a full numerical simulation. Nevertheless, we can derive some conclusions by modelling the SEDs and light curves of the afterglow. We modelled the afterglow SED from NIR to X-ray frequencies at three different epochs, 0.1, 1.0, and 2.18 days, using Xspec v12.12.0 (Arnaud 1996). We have not considered the optical data (z -band and blueward bands) because they are affected by or below the Lyman- α break and thus do not add anything useful to this modelling. The redshift was fixed to 6.312 and we fixed the Galactic and intrinsic hydrogen column density (see § 2.1). To avoid being affected by the uncertain gas absorption, we have not considered data below 0.5 keV in the modelling. We have modelled the NIR-to-X-ray SED both with a single as well as a broken power-law with $\beta_X = \beta_{opt} + 0.5$, at all three epochs. The best-fit parameters are shown in Table 3. All fits give negligible dust extinction $A_V \lesssim 0.03$ mag, independent of the extinction law¹², which is not unusual for (high- z) GRB afterglows (see § 4.7). It is not straightforward to decide between the single and broken power-law models as the SEDs are fit comparably well in both cases. However, we note that in the first epoch they give basically the same value for the low-energy spectral index. Therefore, we conclude that ν_c is within or above the X-ray band at 0.1 d. That ν_c is then in between the two bands is even more clear in the second SED at 1 d whose best-fit gives

¹¹ Two breaks and the peak flux.

¹² In the zdust model.

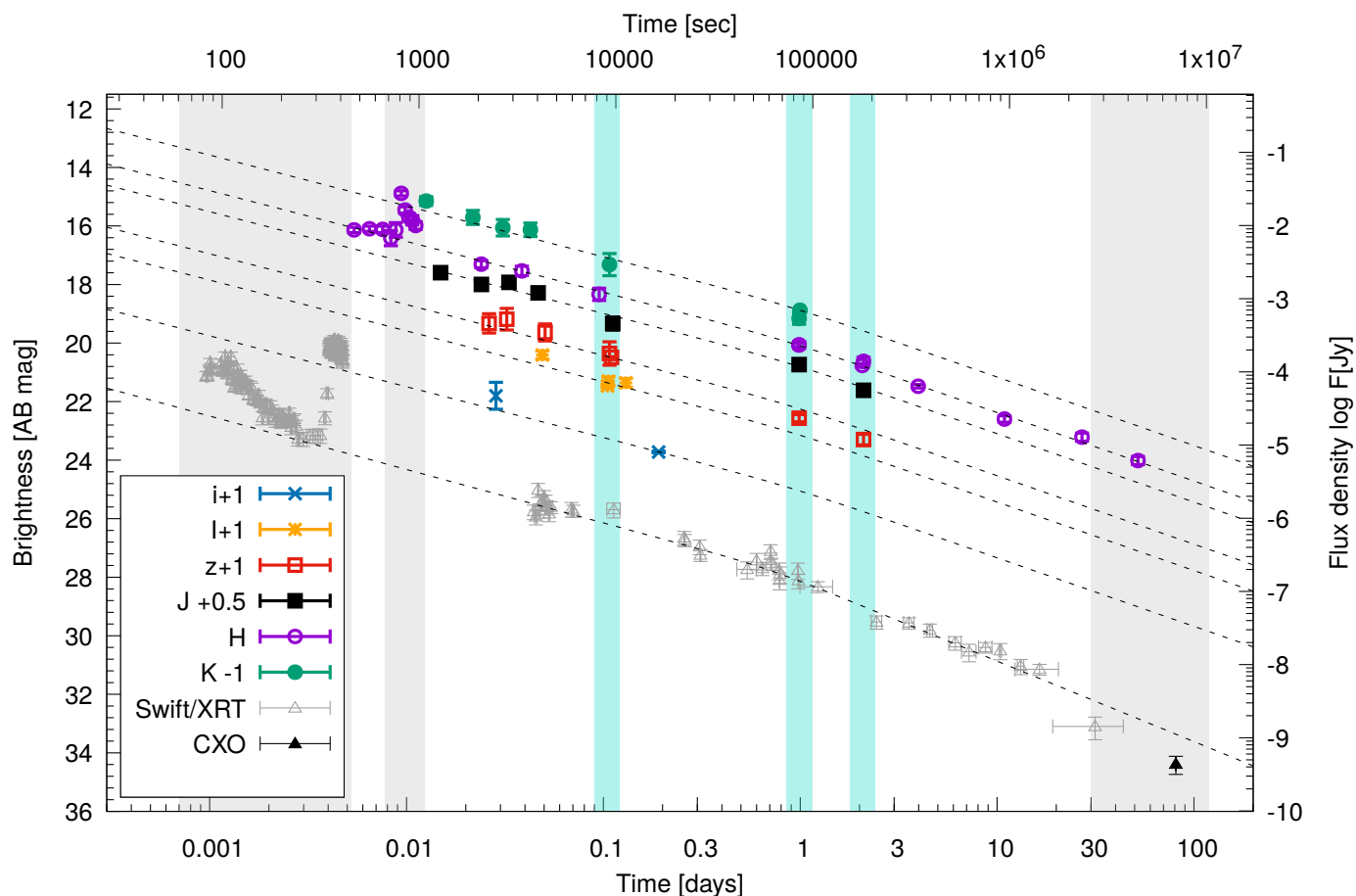


Fig. 3. Optical and X-ray light curves. The dashed lines show the fit to each single band assuming a smoothly broken power-law model. The grey intervals are not considered in the first modelling of the light curves. Those in light blue have been used for the SED fitting (see §3.3). The X-ray light curve is computed at 1.73 keV, the log-mean of the XRT band.

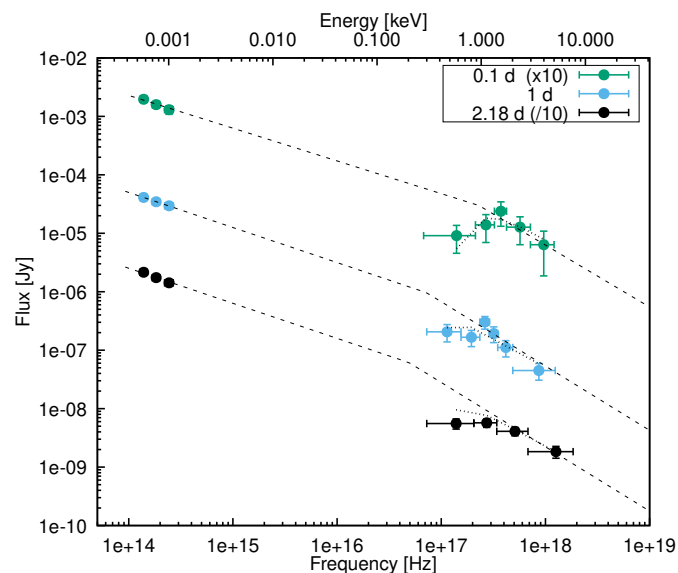


Fig. 4. Optical/NIR to X-ray SEDs of GRB 210905A at three different epochs (0.1, 1.0, 2.18 d). The best fit with a broken power-law is shown in all three epochs, and the best-fit parameters are shown in Table 3 (see §3.3). The dotted- and dashed-lines show the absorbed model and unabsorbed models, respectively.

$\beta_{\text{opt}} = 0.60 \pm 0.04$, and thus an electron index $p = 2.20 \pm 0.08$. To confirm these findings, we need to consider also the light-curve evolution.

We have modelled the optical/NIR light curves simultaneously with a smoothly broken power-law (Beuermann et al. 1999):

$F = (F_1^\kappa + F_2^\kappa)^{-1/\kappa}$, where $F_x = f_{\text{break}}(t/t_{\text{break}})^{-\alpha_x}$, f_{break} the flux density at the break time t_{break} , κ is the break smoothness parameter, and the subscripts 1,2 indicate pre- and post- break, respectively. We find a shallow break with large uncertainty at $t_{\text{break, opt}} = 0.99 \pm 0.73$ d (85.9 ± 62.7 ks) and decay indices $\alpha_{1, \text{opt}} = 0.69 \pm 0.04$ and $\alpha_{2, \text{opt}} = 0.94 \pm 0.04$, with break smoothness $\kappa = 10$ fixed (Zeh et al. 2006)¹³. With respect to a simple power-law, the $\chi^2/d.o.f.$ decreases from 1.36 to 0.92.

The X-ray light curve shows an initial peak at 97s followed by the typical steep decay (Tagliaferri et al. 2005b; Barthelmy et al. 2005b) with $\alpha = 2.37^{+0.15}_{-0.16}$ until ~ 270 s after the burst, when it is interrupted by a flare also visible in gamma-ray data. After ~ 3000 s, it is best modelled by a broken power-law with a shallow break at ≈ 1 d: from $\alpha_{1, X} = 0.74^{+0.03}_{-0.01}$ to $\alpha_{2, X} = 1.10 \pm 0.04$, with $t_{\text{break, X}} = 60 \pm 30$ ks¹⁴ (1σ errors). Finally, we note

¹³ We have also evaluated smaller fixed κ values (5, 2, 1) and find that $\chi^2/d.o.f.$ increases, t_b remains similar, but even at $\kappa = 5$, the error exceeds the value of the break time, and increases further.

¹⁴ As shown by the *Swift*/XRT light curve repository (Evans et al. 2007, 2009).

Table 4. Closure relations.

Afterglow model	Theoretical	Observed	
	α	$\alpha_{1,\text{opt}} = 0.69 \pm 0.04$ $\sigma\text{-level}^{\text{a}}$	$\alpha_{1,\text{X}} = 0.74 \pm 0.03$ $\sigma\text{-level}^{\text{a}}$
ISM; wind, $\nu > \nu_c$	1.15 ± 0.06	6.38	6.11
ISM, $\nu < \nu_c$	0.90 ± 0.06	2.88	2.36
wind, $\nu < \nu_c$	1.40 ± 0.06	-9.76	-11.03
		$\alpha_{2,\text{opt}} = 0.93 \pm 0.04$	$\alpha_{2,\text{X}} = 0.93 \pm 0.04$
ISM, wind, $\nu > \nu_c$	1.15 ± 0.06	3.02	0.69^b
ISM, $\nu < \nu_c$	0.90 ± 0.06	-0.50^b	-2.77
wind, $\nu < \nu_c$	1.40 ± 0.06	-13.17	-15.25

^a The σ -level is the difference of the predicted and the observed temporal slope, normalized to the square root of the sum of their quadratic errors.

^b The solution that matches the closure relations within 1σ is highlighted in bold (see §3.3).

^c We follow the common use and refer to the constant-density medium as ISM.

that modelling simultaneously the X-ray and optical bands with the best-fit indices found above, the shallow break is seen at a common time of 0.70 ± 0.26 days (60.5 ± 22.5 ks).

In Table 4, we compare the observed evolution with the predicted values of the temporal slopes in the optical/NIR and the X-ray bands for various slow-cooling afterglow scenarios (see, e.g., Zhang et al. 2006; Schulze et al. 2011) and the electron index $p = 2.20 \pm 0.08$. We cannot find a good solution for the data before 0.7 d, however, after the first modest break the data are best modelled within a scenario where the jet is expanding into a constant-density medium (hereafter referred to as the interstellar medium or ISM environment). A single power-law SED solution cannot explain the observed temporal decay index in X-rays, $\alpha_{2,\text{X}} = 1.1$, with emission below the cooling frequency, ν_c . Moreover, within this solution β_{opt} should be constant, but instead it evolves with time. These results indicate that ν_c should lie between the optical and X-ray bands (see also Fig. 4). A ν_c that has moved out of the X-ray band can explain the difference in the temporal decay index between optical and X-rays after the shallow break, therefore, we consider a broken power-law as the best description for the optical-to-X-ray SED. For an upper branch¹⁵ $\beta_{\text{X}} = 1.10 \pm 0.04$, obtained at 1d (the epoch with the best statistics), the electron index is $p = 2.20 \pm 0.08$. The large errors on the cooling frequency do not permit to test whether the break shifts in time as $t^{-1/2}$, although the results seem consistent with such a relation (see Table 3).

3.4. Constraints on the jet break

A sizeable number of GRB afterglow light curves break to steeper power-law decays, usually within a few days after the trigger. These breaks have been generally interpreted as due to the outflow being collimated, i.e., a jet, where the break occurs when the relativistic beaming angle becomes wider than the jet's half-opening angle θ_{jet} (Rhoads 1997; Sari et al. 1999). In the forward-shock model the jet breaks have to be achromatic, i.e., have to lead to the same slope (and slope change) simultaneously in all bands¹⁶.

¹⁵ The spectral index $\beta_{\text{X}} = 0.90 \pm 0.15$ at 22.8ks reported in the XRT pages is well in agreement with this result.

¹⁶ The value of the light-curve post-jet-break slope depends on ν_{obs} being above or below ν_m and ν_{sa} , where ν_{sa} is the synchrotron self-

In §3.3 we have shown that a moderate break is present in both optical and X-rays at a common time of ≈ 0.74 d. However, the post-break slope for both X-rays and optical is only ≈ 1 , i.e., too shallow for a jet break, both observationally (Wang et al. 2015) and theoretically (Sari & Piran 1999; Zhang et al. 2006; Panaitescu 2007). Instead, the last XRT detection, together with the late observation by the *Chandra* X-ray Observatory, show that the light curve breaks at ~ 30 d (see also Laskar et al. 2021b). However, the *H*-band light curve, taken up to ~ 52 d, shows no simultaneous steep break (Fig. 3). If we consider that the break in X-rays is indicative of an achromatic break, then the last *H*-band detection must be contaminated by another constant component (see §3.5).

To better constrain the break time, we modelled jointly the *H*-band and X-ray light curves after the early break at 0.7 d with a smoothly broken power-law $F = (F_2^\kappa + F_3^\kappa)^{-1/\kappa}$, following to the definition in §3.3 but with the subscripts 2, 3 indicating the pre- and post-jet break respectively. We fixed the pre-jet-break index to the model values $\alpha_{2,\text{opt}} = 0.9$ and $\alpha_{2,\text{X}} = 1.15$ (see Table 4). In our analysis we adopt the jet model (with sideways expansion) and slow cooling (e.g., Sari et al. 1998; Zhang & Mészáros 2004). Therefore, we assume that the post jet-break index is $\alpha_{3,\text{opt}} = \alpha_{3,\text{X}} \approx p = 2.2$ (see §3.3). Note that the sparse data after the break prevents us from constraining the κ parameter. Therefore, we let it vary between the two extremes of the interval $1 < \kappa < 5$. These are consistent with the expected value for emission either side of ν_c and for a typical GRB observation angle (van Eerten & MacFadyen 2013; Lamb et al. 2021). Note that from the models, it is difficult to get $\kappa > 5$ (van Eerten & MacFadyen 2013). In *H*-band we added an additional constant component. In summary, the only free parameters are the break time, the flux at the jet break and the flux of the constant source. The best-fit break time is¹⁷ $t_{\text{jet}} = 38.8 \pm 21.1$ d with a constant source with $H_{\text{AB}} = 24.9 \pm 0.6$ mag. The modelling is shown in Fig. 5.

3.5. The nature of the *H*-band flattening at late times

The contaminating source could be a (or part of a) compact galaxy along the line-of-sight. In Fig. 6 we show the region around the ALMA localization in a deep Bessel *I*-band imaging observation obtained 87 d after the GRB with the VLT/FORS2 instrument. A faint foreground source with $I_{\text{Bessel}} = 24.84 \pm 0.18$ mag (AB) lies $1''.5$ away from the GRB and could possibly extend over its position. Its contribution to the GRB location is uncertain ($I_{\text{Bessel}} = 26.15 \pm 0.40$ mag) and it is not detected in *r'*- and *g'*-band X-shooter imaging down to ~ 25 mag. We cannot exclude that this object contributed to the flux in the *H*-band. Such an object could also be responsible for the foreground intervening system that we have found in X-shooter spectra at $z = 2.8$ with high-EW Mg II absorption (see Saccardi et al. in prep.). In this case, the cold gas observed in absorption can also be offset from the hot and bright region observed in *I*-band, or occupy a larger region of the same foreground galaxy. Of course, at least part of the flux should come from the host galaxy of the GRB. A host galaxy at $z = 6.3$ with observed $H \sim 25$ mag, and thus a rest-frame UV luminosity of $L_{\nu} = 2.33 \times 10^{29}$ ergs $\text{s}^{-1} \text{Hz}^{-1}$, would have a SFR $\gtrsim 30 M_{\odot} \text{yr}^{-1}$ using equation 1 in Kennicutt (1998). This is certainly possible

absorption frequency. Optical and X-ray afterglow SEDs are usually observed to be above ν_m (e.g., Greiner et al. 2011).

¹⁷ Assuming no sideways expansion, and thus $\alpha_3 = \alpha_2 + 3/4$ (Panaitescu 2007), we find a similar solution $t_{\text{jet}} = 36.4 \pm 21.6$ d.

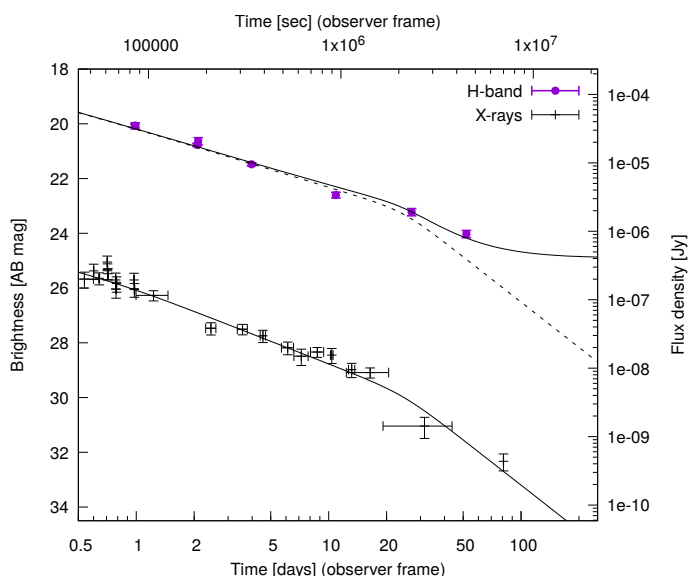


Fig. 5. Observer-frame H -band (purple) and X-ray (black) light curves. Solid lines show the joint fit with a smoothly-broken power-law, assuming common achromatic breaks. The dashed line shows the H -band light curve without constant component. Following the slow-cooling scenario (§3.3), we fixed the pre-break decay indices to $\alpha_{opt} = 0.87$ and $\alpha_X = 1.12$. The last break is interpreted as a jet break, and thus the post-break decay index has been fixed to $\alpha_{opt,X} = p = 2.2$. The late flattening in the H -band light curve can be explained by a constant contribution from a host or intervening system. See §3.4 for details.

(see also the discussion in Saccardi et al. in prep.), and in fact McGuire et al. (2016) find that the $z \gtrsim 6$ GRB hosts known to date (those of GRBs 050904, 130606A, and 140515A) likely have similar or slightly lower SFR, assuming a short-lived burst of star-formation (see also Tanvir et al. 2012). However, given the presence of the foreground source noted above, the host can be fainter and thus the inferred SFR is just an upper limit. Future observations ($HST/JWST$) will help to further untangle the different contributions to the late afterglow.

4. Discussion

4.1. The nature of the prompt emission

GRB 210905A is among the few exceptional cases where optical data could be obtained during a gamma-ray pulse (Fig. 1). In the past, in less than a dozen cases, has modelling of the prompt emission been possible from optical/NIR to gamma-rays, like in the cases of GRBs 990123, 041219A, 060526, 080319B, 080603A, 080928, 090727, 091024, 110205A, 111209A, 130427A, and the more recent GRBs 160625B and 180325A (e.g., Sari & Piran 1999; Vestrand et al. 2005; Thöne et al. 2010; Racusin et al. 2008; Guidorzi et al. 2011; Rossi et al. 2011; Kopač et al. 2013; Virgili et al. 2013; Stratta et al. 2013; Kann et al. 2011; Zheng et al. 2012; Gendre et al. 2013; Vestrand et al. 2014; Troja et al. 2017; Becerra et al. 2021).

At $z > 6$, this analysis was possible only for the 16 year-old GRB 050904 (Boër et al. 2006). In all these cases, modelling of the data with a broken power-law shows that the X-to-gamma-ray SED of the prompt pulses is in agreement with synchrotron emission, and in particular with fast cooling. This is in agreement with studies on large samples as we have mentioned in § 3.2 (see Ghisellini et al. 2020, for a discussion on the possible implications).

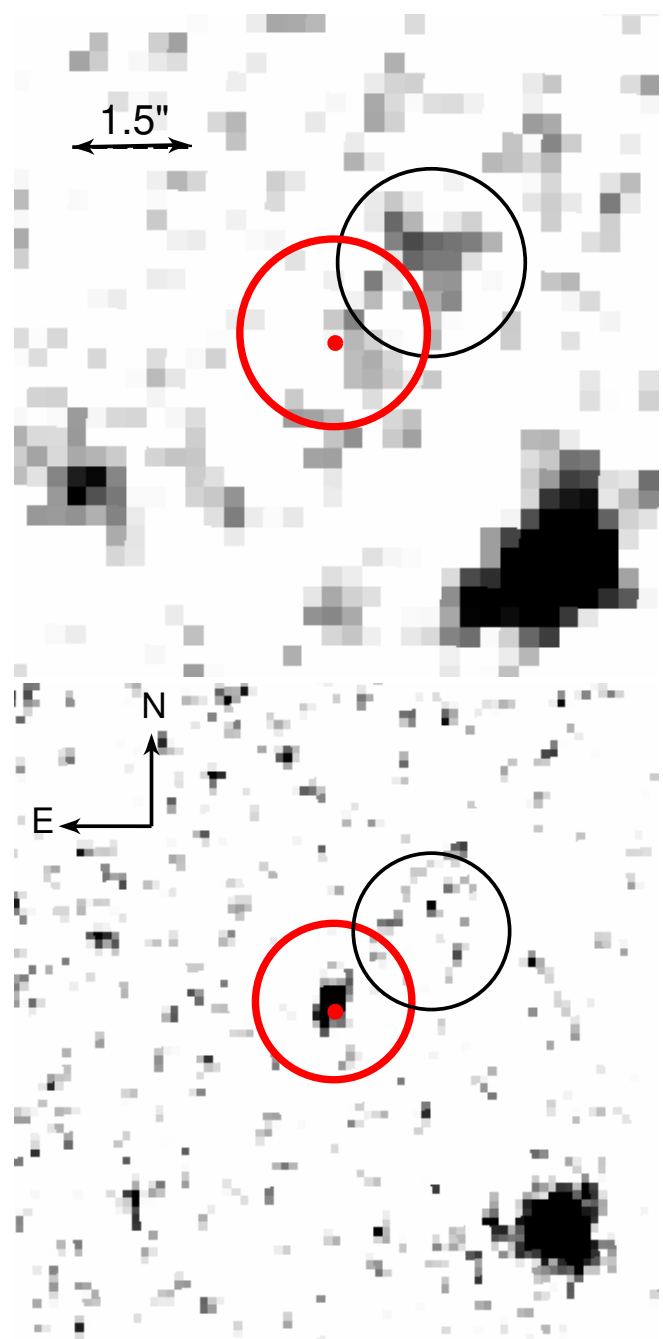


Fig. 6. *Top:* Zoom-in on deep FORS2 I_{Bessel} -band image obtained 87 d after the GRB trigger. The red point indicates the ALMA localization of the afterglow. A faint source, highlighted with a black circle, lies ~ 1.5 away from the GRB. The radius of the circles is that of the aperture used for photometry. *Bottom:* For comparison, the faint source is not visible in the black circle in last H-band at 52 d.

However, when including the optical data the situation can be more complex: for example, the main and earlier pulses of GRBs 990123 (Sari & Piran 1999; Galama et al. 1999; Corsi et al. 2005; Maiorano et al. 2005), 080319B (Racusin et al. 2008; Bloom et al. 2009), 111205A (Zheng et al. 2012), 130427A (Vestrand et al. 2014), 160625B (Troja et al. 2017), and 180325A (Becerra et al. 2021) show a convex spectrum between optical and X/gamma-rays. Although, different interpretations are also possible (e.g., Guiric et al. 2016), this feature can be explained by synchrotron emission from internal forward shocks dominat-

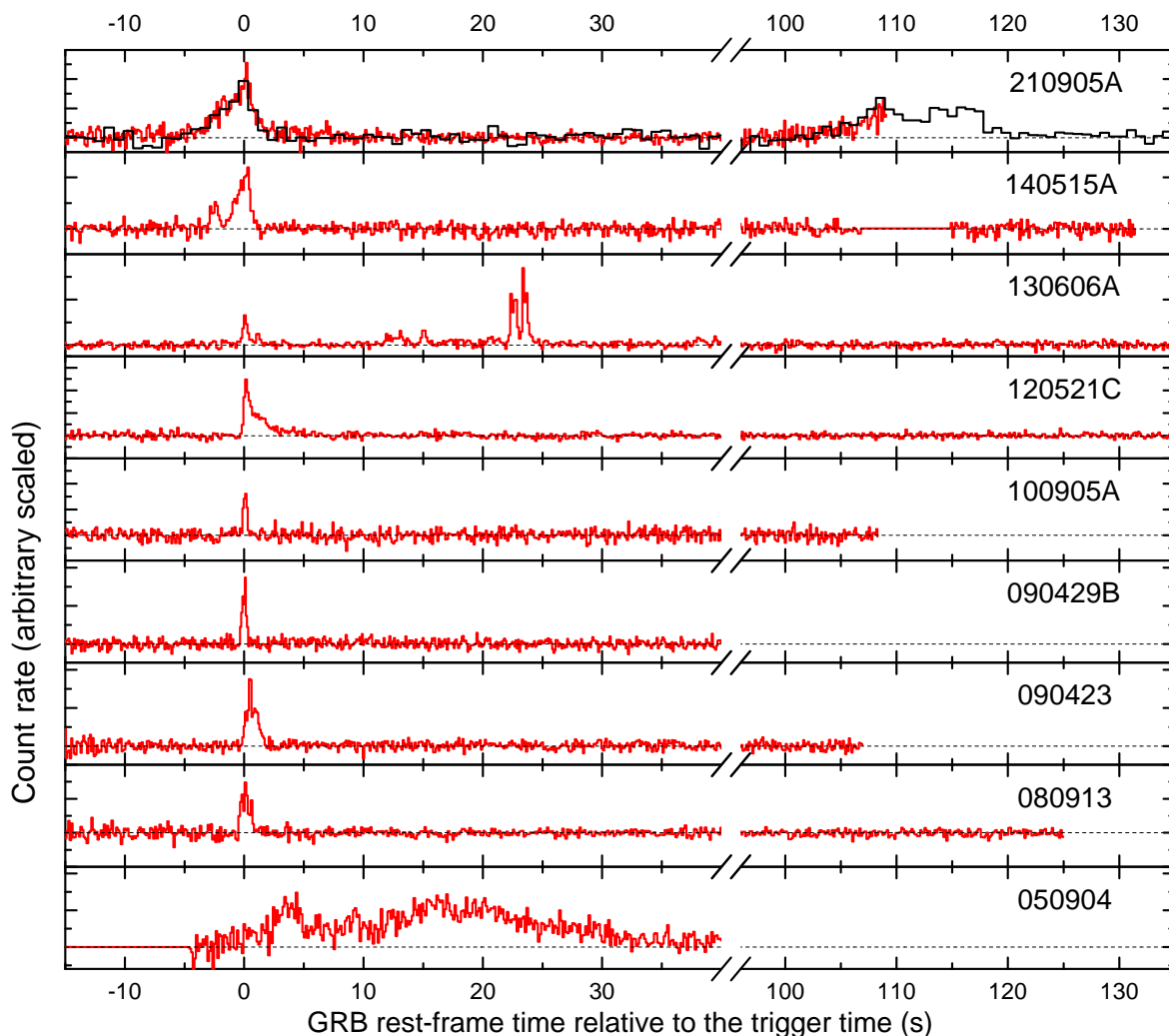


Fig. 7. GRB 210905A prompt-emission light curve (top panel) in the context of eight high-redshift GRBs ($z \geq 6$). Arbitrarily scaled BAT count rates (15 – 350 keV) are plotted in red against time in the GRB rest frame. The KW light curve of GRB 210905A is plotted in black.

ing the gamma-ray and X-ray prompt emission, while the early optical flashes are generated by a reverse shock.

The analysis of the Pulse 3 of GRB 210905A is however clearly in disagreement with this latter scenario, with the H -band emission being fainter than the extrapolation of the power-law modelling the gamma-rays (Fig. 2). Therefore, although simultaneous optical-to-gamma coverage of the first prompt pulses is missing in the case of GRB 210905A, we show that at least during the last pulse there is no indication that the NIR data have a different origin than the X/gamma-ray emission, and all the observed epochs during the prompt phase can be explained by synchrotron emission from internal shocks. This is not surprising, as in several events (e.g., GRBs 990123, 130427A, 160525B) the optical-to-gamma SED later evolves and can be entirely explained as emission from the forward shock. Oganessian et al. (2019) have shown that the later SEDs are consistent with being produced through synchrotron emission in the moderately fast-cooling regime from the same emission region.

4.2. Prompt emission in context

Using $z = 6.312$, we estimate the rest-frame properties of the burst prompt emission. Isotropic-equivalent energy release (E_{iso}) and rest-frame spectral peak energies $E_{\text{peak},z} = (1+z)E_{\text{peak}}$ for the individual emission episodes were calculated from the CPL spectral fits (§3.1); they are listed in Table 5. Integrated over the three intervals, the total energy release of GRB 210905A in γ -rays is $E_{\text{iso}} = 1.27^{+0.20}_{-0.19} \times 10^{54}$ erg, which is within the highest $\sim 7\%$ for the KW sample of 338 GRBs with known redshifts (Tsvetkova et al. 2017, 2021). The reported values of E_{iso} and L_{iso} were calculated in the rest frame 1 keV–10 MeV range. All the quoted errors are at the 1σ confidence level. Since E_{peak} obtained from our fits differs between the individual emission episodes, we used the spectral peak energy value weighted by the episode fluence, $E_{\text{peak}} \sim 145$ keV, to estimate the burst time-averaged $E_{\text{peak},z}$ to ~ 1060 keV. This intrinsic peak energy is among the highest $\sim 15\%$ of long KW GRBs. Derived from the peak energy flux, the peak γ -ray luminosity of the burst is $L_{\text{iso}} = 1.87^{+0.36}_{-0.26} \times 10^{53}$ erg s^{-1} . The rest-frame E_{peak} corresponding to the time interval around the peak luminosity is ~ 1050 keV.

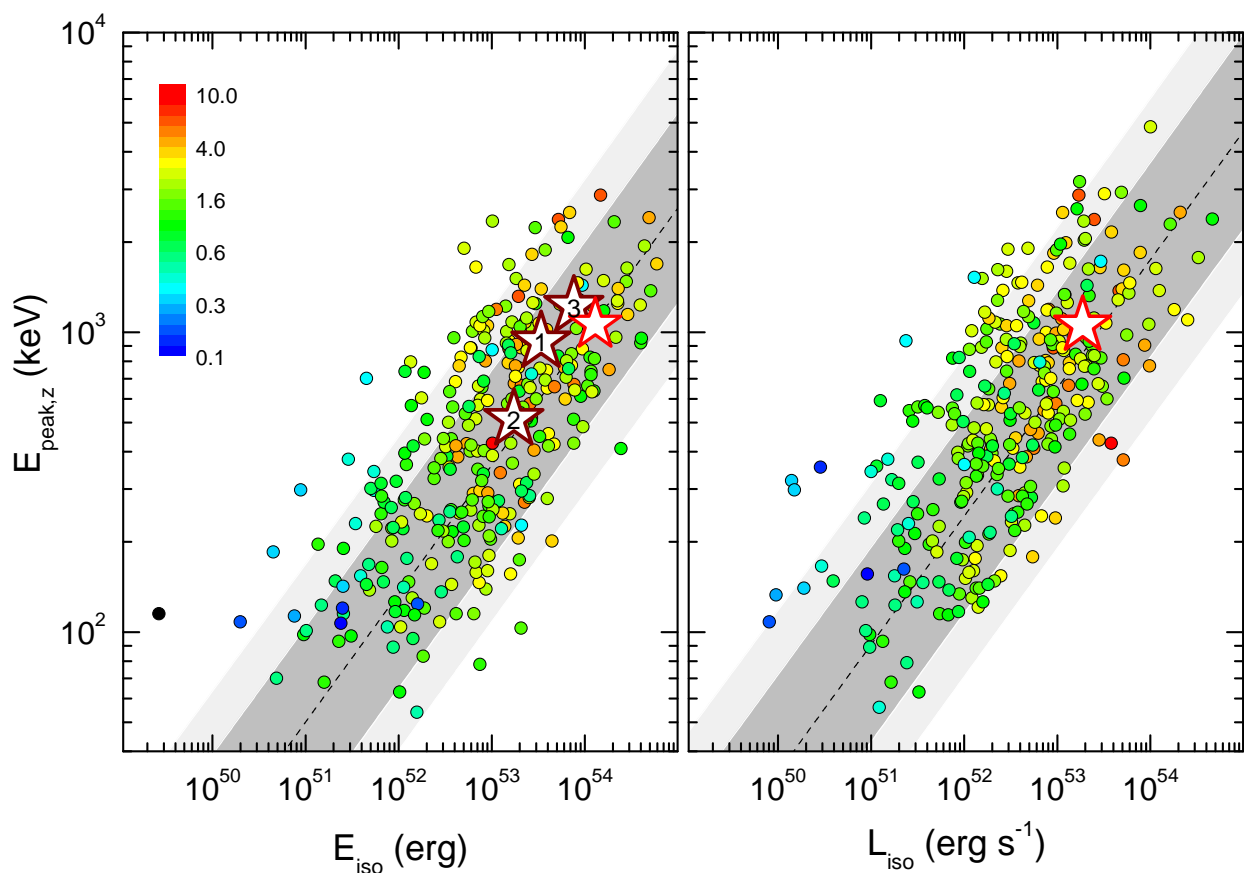


Fig. 8. Rest-frame energetics of GRB 210905A in the $E_{\text{peak},z}-E_{\text{iso}}$ and $E_{\text{peak},z}-L_{\text{iso}}$ planes (red stars). Brown stars in the left panel show the values derived for the individual Pulses 1, 2, and 3. The rest-frame parameters of 315 long KW GRBs with known redshifts (Tsvetkova et al. 2021) are shown with circles; the color of each data point represents the burst’s redshift. The “Amati” and “Yonetoku” relations for this sample are plotted with dashed lines and the dark- and light-gray shaded areas show their 68% and 90% prediction intervals, respectively. The error bars are not shown here for reasons of clarity.

With these estimates, GRB 210905A as well as its individual episodes lie inside the 68% prediction interval (PI) of the $E_{\text{peak},z} - E_{\text{iso}}$ (“Amati” relation; Fig. 8) for 315 long KW GRBs with known redshifts (Tsvetkova et al. 2021). Likewise, the burst peak luminosity and the corresponding $E_{\text{peak},z}$ perfectly fit the “Yonetoku” relation for the sample.

Figure 7 shows the GRB 210905A prompt emission in the context of eight GRBs at $z \gtrsim 6$. With the rest-frame duration $T_{90}/(1+z) \sim 119$ s GRB 210905A is the intrinsically longest high- z GRB detected to date and is also among the longest $\sim 3\%$ of bursts as compared to the whole KW catalog¹⁸ (Tsvetkova et al. 2017, 2021), which covers the range $0.04 \leq z \leq 9.4$. s In this high-redshift sample, GRBs 210905A and 130606A are the only bursts with well-separated emission episodes. Except for this feature, they are similar to all other bursts which show short spikes with only moderate energy release. The exception is GRB 050904, which is similar to GRB 210905A in terms of energy released ($E_{\text{iso}} = 1.33 \pm 0.14 \times 10^{54}$ erg) but shows a ~ 30 s long emission episode with two extended peaks (and at least a third episode observed in X-rays).

The most powerful burst at low redshift is GRB 130427A at $z = 0.3399$ (Selsing et al. 2019). This GRB can be considered as a good analog of the energetic high- z population because of its high energy release (Perley et al. 2014; De Pasquale et al.

2016). Its prompt emission parameters are similar to those of Pulse 3 of GRB 210905A (see Tab. 5): $E_{\text{peak},z} \sim 1415$ keV and $E_{\text{iso}} \sim 9.4 \times 10^{53}$ erg (Tsvetkova et al. 2017). Accordingly, GRB 130427A and Pulse 3 lie very close in the $E_{\text{peak},z} - E_{\text{iso}}$ plane. We should note, however, that the intrinsic durations of GRB 130427A and pulse 3 of GRB 210905A differ by factor of two ($T_{90,z} \sim 10$ s for GRB 130427A versus ~ 19 s for Pulse 3). The initial light curve of GRB 130427A is somewhat similar to that of GRB 210905A as it starts with a large structured peak ~ 20 s long in the rest-frame, followed by a third peak starting at ~ 100 s. This second pulse is, however, orders of magnitude weaker than the main pulse. So, GRB 130427A is not a “genuine” multi-episode GRB like this work’s burst or GRB 130606A, and is instead more similar to the other high-redshift GRBs.

4.3. Collimation-corrected energy and central engine

Knowing the value of the jet opening angle is crucially important because it enables us to estimate the “true”, collimation-corrected, energetics of the outflow (Frail et al. 2001; Ghirlanda et al. 2007). Numerical and analytical calculations (e.g., Sari et al. 1999) have shown that the half-opening angle of the jet is related to the jet-break time. Following Zhang & MacFadyen (2009) we calculate this angle θ_{jet} using the following equation

¹⁸ This sample does not include six KW ultra-long ($T_{100} > 1000$ s) bursts, all at low-to-moderate redshifts $z \lesssim 2$.

Table 5. Parameters of the individual prompt emission pulses.

Episode	$E_{\text{peak},z}$ (keV)	Fluence(15 – 1500 keV) ^a 10^{-5} erg cm ⁻²	E_{iso} (10^{53} erg)
Pulse 1	930 ⁺²³⁰ ₋₁₄₀	0.471 ^{+0.052} _{-0.046}	3.40 ^{+0.41} _{-0.33}
Pulse 2	510 ⁺¹⁶⁰ ₋₉₅	0.245 ^{+0.050} _{-0.035}	1.73 ^{+0.37} _{-0.33}
Pulse 3 ^b	1220 ⁺⁶⁴⁰ ₋₄₅₀	1.11 ^{+0.28} _{-0.26}	7.62 ^{+1.89} _{-1.81}
Total ^c	1060 ⁺⁴⁷⁰ ₋₃₂₀	1.82 ^{+0.29} _{-0.28}	12.7 ^{+2.0} _{-1.9}

^a Fluences were calculated using the fits with the CPL function from Table 2.

^b Only the KW 3-channel spectrum is used.

^c This fluence is integrated over all three emission episodes.

for a uniform jet expanding in a constant-density medium:

$$\theta_{\text{jet}}[\text{rad}] = 0.12 \left(\frac{E_{\text{kin,iso}}}{10^{53} \text{ ergs}} \right)^{-1/8} \left(\frac{n}{\text{cm}^{-3}} \right)^{1/8} \left(\frac{t_{\text{jet}}}{\text{days}} \right)^{3/8} (1+z)^{-3/8} \quad (1)$$

where $E_{\text{kin, iso}}$ is the kinetic energy of the outflow assuming isotropy; $n = 1 \text{ cm}^{-3}$ is the density of the medium in particles, assumed to be constant; t_{jet} is the jet-break time in days (observer frame, see §3.4), while $z = 6.312$ is the redshift of the event. The kinetic energy is the one left after the prompt phase, and which later dissipates in the afterglow. Together with the energy released as gamma-rays in the prompt phase¹⁹ $E_{\gamma, \text{ iso}}$, it represents part of the total GRB fireball energy $E_{\text{total, iso}} = E_{\text{kin, iso}} + E_{\gamma, \text{ iso}}$ (e.g., Zhang & Mészáros 2004; De Pasquale et al. 2016). Assuming an efficiency²⁰ $\eta = E_{\gamma, \text{ iso}}/E_{\text{total, iso}} = 0.2$ we derive $\theta_{\text{jet}} = 0.137 \pm 0.028$ rad, or 7.87 ± 1.60 degrees. If we consider that the outflow is collimated, the “true” gamma-ray energy of the jet is $E_{\gamma} = E_{\gamma, \text{ iso}} (1 - \cos(\theta_{\text{jet}})) \approx 1 \times 10^{52}$ erg. The assumed efficiency is justified theoretically (e.g., Guetta et al. 2001) and by recent studies of GRB afterglows in the optical, X-rays and GeV gamma-rays (e.g., Beniamini et al. 2015). However, higher values are also possible, as suggested by some observations (Zhang et al. 2007a; Lü et al. 2018) and theoretical models (e.g., Kobayashi & Sari 2001; Zhang & Yan 2011). As shown in De Pasquale et al. (2016), the minimum E_{total} is obtained for $\eta = 3/4$. Lower efficiencies correspond to higher total energies. Therefore, with $\eta = 0.2-0.75$ we can estimate the *total collimated energy* of the jet to be $E_{\text{total}} \approx E_{\gamma}/\eta \approx 2-6 \times 10^{52}$ erg. We note that the dependence of θ_{jet} on n and the kinetic energy is rather weak (Eq. 1). Thus, the total energy is not sizeably affected by the exact values of n and E_{kin} ²¹.

The most widely discussed models of central engines of GRBs are accreting magnetars or accreting black holes. We can assume for a standard neutron star with mass $M \sim 1.4 M_{\odot}$ the maximum rotation energy to be in the range 3×10^{52} erg (Lattimer & Prakash 2016) – 7×10^{52} erg (Haensel et al. 2009). Therefore, our analysis allows us to disfavor a standard magnetar as central engine of this GRB. Only the most extreme magnetar models with $M \gtrsim 2.1 M_{\odot}$ and rotation energy $\sim 10^{53}$ erg are not excluded (see Metzger et al. 2015; Dall’Osso et al. 2018; Stratta et al. 2018). On the other hand, according to the Kerr metric

¹⁹ Here, $E_{\gamma, \text{ iso}}$ is the same as $E_{\text{iso}} = 12.7 \times 10^{53}$ erg of §4.2.

²⁰ And thus $E_{\text{kin, iso}} = (1/\eta - 1) E_{\gamma, \text{ iso}}$.

²¹ The density n can be orders of magnitude larger (e.g., Laskar et al. 2018), but this would just cause an even larger θ_{jet} and E_{total} (Cenko et al. 2011; Granot & van der Horst 2014).

(Kerr 1963) the rotational energy E_{rot} of a black hole can reach up to 29% of its total mass, which exceeds that of neutron stars by a full order of magnitude. Indeed, rotating black holes of mass $M \sim 3 M_{\odot}$ possess rotational energies up to $E_{\text{rot}} \sim 10^{54}$ erg (e.g., van Putten & Della Valle 2017). Therefore, an energy budget of $\sim 10^{53}$ erg can be conveniently extracted via the Blandford-Žnajek mechanism (Blandford & Žnajek 1977), thereby suggesting that the central engine of GRB 210905A may well be a rotating black hole.

4.4. The early X-ray and optical/NIR afterglow

As shown in §3.3, although the optical-to-X-ray SED at 0.1 d is in agreement with the cooling break lying within the X-ray band, both their light curves are not well explained by the standard fireball scenario before the common shallow break at ~ 0.7 d. Here, we can investigate whether our data can justify the early decay and the shallow break.

First, the early break at ~ 0.7 d is not well-constrained but we can exclude that it is due to a wind-to-constant-density transition as the light-curve decline, in such a scenario, would become shallower and not steeper (e.g., Panaitescu 2007; Schulze et al. 2011). The times and the slopes instead make it an example of a “canonical” GRB X-ray afterglow light curve (Nousek et al. 2006; Zhang et al. 2007b). Studying the canonical light curve, Zhang et al. (2007b) interpreted the break between the shallow segment with $\alpha \approx 0.7$ to the more “normal” segment with $\alpha \approx 1$ as the end of an “energy injection” phase. During energy injection, the ejecta is still receiving energy, either from a long-lived central engine, or by slower ejecta shells that catch up with the leading shell. In other words, the mild break should be interpreted as cessation of energy injection. Following the relations in Zhang et al. (2006), where q the energy injection index, we have (for ISM and $p = 2.2$): $\alpha_{\text{opt}} = ((2p - 6) + (p + 3)q)/4$, from which follows $q = 0.84$ and $\alpha = 0.69$ for $\nu < \nu_c$; for X-rays we obtain $\alpha_X = ((2p - 4) + (p + 2)q)/4$, so $q = 0.84$, and $\alpha = 0.98$ for $\nu > \nu_c$. Using a stratified shell model with ejected mass $M(> \gamma) \propto \gamma^{-s}$, where γ is the Lorentz factor of the shell (Rees & Mészáros 1998) and the relation between s and q parameters ($s = (10 - 7q)/(2 + q)$, Zhang et al. 2006), we find that a value of $s \sim 1.45$ fits the pre-break behavior. Equally, a magnetar central engine model that continuously injects energy as $L(t) \propto t^{-q}$ (e.g., Dai & Lu 1998), can model the early decay with $q = 0.84$. Therefore, we cannot discard one model over the other, i.e., stratified shell versus magnetar. However, as discussed in §3.4 the energy constraints likely limit the viability of a new-born magnetar as the power source of the energy injection.

We note also that the energy-injected $\alpha_{X,1} \sim 0.98$ is larger than the value observed (0.74). However, this theoretical value assumes $\nu > \nu_c$ but in Table 3 we see that ν_c is well within the X-ray band in the first day after the burst trigger. The energy injection changes the way the cooling frequency evolves, i.e., $\nu_c \propto t^{(q-2)/2} = t^{-0.58}$ for $q = 0.84$, and thus the cooling frequency evolves slightly faster whilst energy injection is happening: if the cooling frequency is at ~ 2 keV at 0.1 d, then at 1 d it would have been at 0.5 keV, and consistent with what we observe. Moreover, one should also consider that the ν_c break is likely smooth and covers a relatively large interval (e.g., Granot & Sari 2002). Therefore, the observed temporal decay index may well be somewhere between the values predicted for the $\nu < \nu_c$ and the $\nu > \nu_c$ cases, i.e. $0.69 < \alpha_{X,1} < 0.98$, in agreement with the observed value before ~ 70 ks.

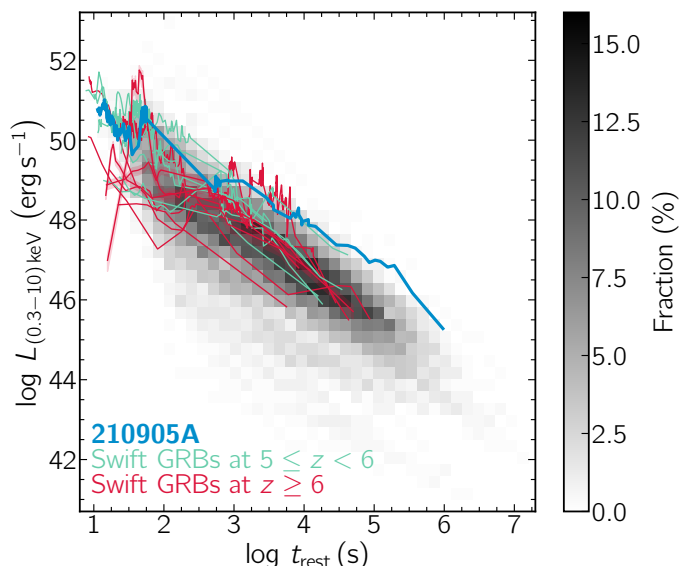


Fig. 9. The X-ray afterglow of GRB 210905A (blue line) in the context of other high-redshift GRBs (green and red) and the world-sample of *Swift* GRBs with known redshifts (grey density plot). The afterglow of GRB 210905A is the brightest after 10 ks among all $z > 5$ GRBs and one of the brightest in general. The color table on the right side translates a grey shade at a given luminosity and time into a fraction of bursts.

4.5. The X-ray afterglow in context

To put the X-ray emission in the context of other GRB afterglows, in particular high-redshift GRBs, we retrieved from the *Swift* Burst Analyser (Evans et al. 2010) the X-ray light curves of 454 long-duration *Swift* GRBs with detected X-ray afterglows (detected in at least two epochs) and known spectroscopic redshifts, which were discovered before the end of December 2021. We processed the data and moved them to their rest-frames following Schulze et al. (2014). In addition we retrieved the X-ray light curves of the high-redshift GRBs 090423, 090429B and 100905A that have only a photometric redshift. Fig. 9 shows the parameter space occupied by long-duration GRBs as a density plot and the X-ray light curve of GRB 210905A in blue. The uncertainty in their luminosity is indicated by shaded regions around the light curves at their redshifts.

GRB 210905A’s X-ray afterglow is among the most luminous at all times. Even compared to other GRBs at $5 < z < 6$ (green; GRBs 060522, 060927, 130606A, 131227A, 140304A, 201221A) and $z > 6$ (red; 050904, 080913, 090423, 090429B, 100905A, 120521C, 120923A, 140515A), GRB 210905A has an exceptionally high luminosity. Furthermore, its X-ray afterglow is fading slower than those of most GRBs, at least until the jet break at $\sim 5 \times 10^5$ in the rest frame (§3.4). Here we note that some of the other bursts at high- z do not show a clear light-curve break in X-rays (GRBs 050904, 080913, 090423, 130606A), although some of them show a break in the optical (GRBs 050904, 090423, 090429B, 120521C), and GRB 140515A has just one single detection that suggests a possible break like GRB 210905A. This is because of the low observed flux of these very high- z afterglows, as only the most luminous events are bright enough for *Swift*/XRT.

4.6. The optical/NIR afterglow in context

Following the method devised in Kann et al. (2006), we are able to put the NIR afterglow into the context of the (optical/NIR) total afterglow sample. We derive the observer-frame R_C magnitude by shifting all data to the H band, then extrapolating the spectral slope into the observer-frame R_C band, which is completely suppressed at the redshift of the GRB (assuming that there would be no Lyman absorption). The spectral slope, redshift, and the lack of extinction are then used to derive the magnitude shift $dR_C = -5.12^{+0.20}_{-0.21}$ mag to $z = 1$. The derived R_C -band light curve still represents an observed magnitude, it is as if the GRB were at $z = 1$ in a completely transparent universe.

We then compare the afterglow with the GRB afterglow light curve samples of Kann et al. (2006, 2010, 2011) as well as samples from upcoming publications (Kann et al., 2022a,b,c, in prep.). The result is shown in Fig. 10, with GRB 210905A highlighted in red. The sample of Kann et al. (2022a), in prep. focuses on $z \gtrsim 6$ GRBs, and these light curves are highlighted as thick black curves. At early times, the afterglow of GRB 210905A is seen to be among the most luminous known, albeit still fainter than the early afterglows of high- z GRBs 130606A and especially 050904 (Kann et al. 2007). Interestingly, the early flash of GRB 210905A aligns well in rest-frame time (between 70 and 110 s) with those seen in GRB 050904 (Boër et al. 2006), GRB 160625B (Troja et al. 2017, an extremely energetic lower-redshift GRB, seen behind GRB 050904 in the plot), and, with less contrast, in GRB 130606A (Castro-Tirado et al. 2013). On the other hand, several bright prompt-associated flashes happen significantly earlier, such as the cases of GRB 080319B (Racusin et al. 2008; Bloom et al. 2009) and GRB 120711A (Martin-Carrillo et al. 2014, Kann et al. 2022a, in prep.). Therefore, this similarity in time is likely just a chance coincidence.

The most intriguing result is found at the end of the light curve. Even after removing the potential constant component, the combination of a late break and an early shallow decay makes the afterglow of this burst one of the most luminous ever detected at such late times (overlapping with that of GRB 160625B within errors, Kann et al. 2022b, in prep.), providing further evidence for the extremely energetic nature of the event.

4.7. Dust absorption and equivalent hydrogen column densities

Like other high- z bursts (see e.g., Zafar et al. 2010, 2011, 2018; Melandri et al. 2015), GRB 210905A is characterized by negligible absorption in the optical/NIR, in agreement with those expected for high- z galaxies populating the faint end of the luminosity function (e.g., Salvaterra et al. 2011). In particular, McGuire et al. (2016) studied three $z > 5.9$ GRB hosts and noted that afterglow analyses in each case pointed to low line-of-sight dust extinction.

Although a low A_V is expected to correlate with a low $N_{H,X}$, the high $N_{H,X}$ value of $7.7^{+3.6}_{-3.2} \times 10^{22} \text{ cm}^{-2}$ is also not exceptional. It is also observed in other environments, like in AGNs, and can be naturally explained by the absorption of intervening metals along the line-of-sight (Starling et al. 2013; Campana et al. 2015), which reside almost entirely in the neutral gas at $z > 4.5$ (e.g., Péroux & Howk 2020), although one cannot exclude the contribution of increasing gas density in the vicinity of the GRB (Heintz et al. 2018). The high $N_{H,X}$ is also in contrast with the $N_{\text{H}i} \simeq 1.35 \times 10^{21} \text{ cm}^{-2}$ measured via the Lyman- α absorption-line by Fausey et al. (in prep.). The difference can be explained by the very high number of ionizing photons produced by the

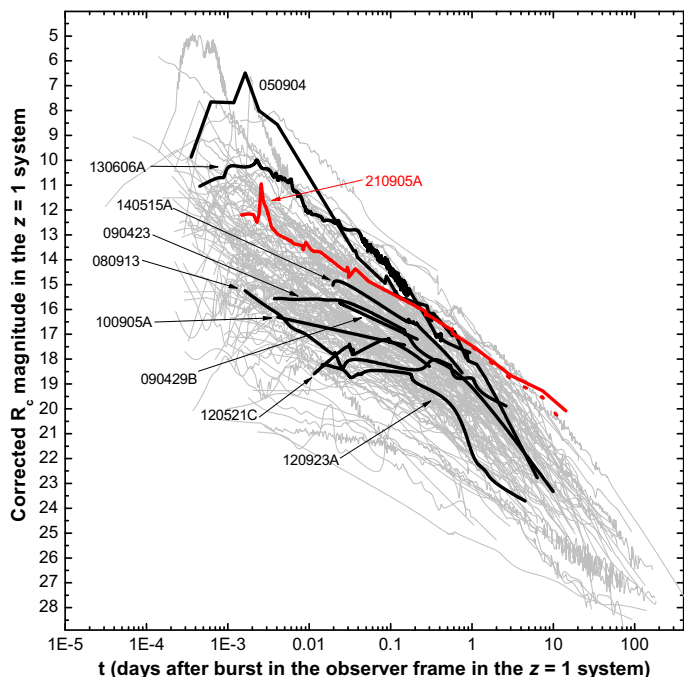


Fig. 10. The optical afterglow of GRB 210905A (red line) compared to a sample of extinction-corrected afterglows which have all shifted to $z = 1$, from Kann et al. (2006, 2010, 2011, 2022a,b,c, in prep.). Hereby, time and magnitudes are given in the observer frame, but assuming all GRBs are at $z = 1$ in a perfectly transparent universe. Light gray are LGRBs, thicker black lines GRBs with redshifts $z \geq 6$. All magnitudes are Vega magnitudes. The afterglow of GRB 210905A is the brightest afterglow ever detected at late times. Even if the potential constant source (§3.5) is subtracted (red dotted line), the afterglow is still among the most luminous ever detected, next to that of GRB 160625B.

GRB that could ionize the IGM along the line-of-sight up to several hundreds of kpc (Saccardi et al. in prep.). We discuss the IGM contribution in more detail in Fausey et al. (in prep.).

4.8. X-ray afterglow luminosity versus prompt energy

As already shown by De Pasquale et al. (2006) (see also Nysewander et al. 2009) the X-ray luminosity and the isotropic gamma-ray energy release seem to broadly follow a linear relation, suggesting a roughly universal efficiency for converting a fraction of the initial kinetic energy²² into gamma-ray photons. This was later further confirmed by D’Avanzo et al. (2012). GRBs at $z > 6$ also follow this relation. We test here whether GRB 210905A follows this relation despite its luminosity. We estimate the afterglow X-ray integral flux in the 2 – 10 keV rest-frame common energy band and compute the corresponding rest-frame X-ray luminosity at different rest-frame times. The 2 – 10 keV rest-frame flux was computed from the observed integral 0.3 – 10 keV unabsorbed fluxes and the measured photon index, Γ (which we retrieved from the online *Swift* Burst Analyser, Evans et al. 2009, 2010) in the following way (see Gehrels et al. 2008; D’Avanzo et al. 2012):

$$f_{X,rf}(2 - 10 \text{ keV}) = f_X(0.3 - 10 \text{ keV}) \frac{\left(\frac{10}{1+z}\right)^{2-\Gamma} - \left(\frac{2}{1+z}\right)^{2-\Gamma}}{10^{2-\Gamma} - 0.3^{2-\Gamma}} \quad (2)$$

²² To not be confused with E_{kin} , which is the energy left after the prompt phase.

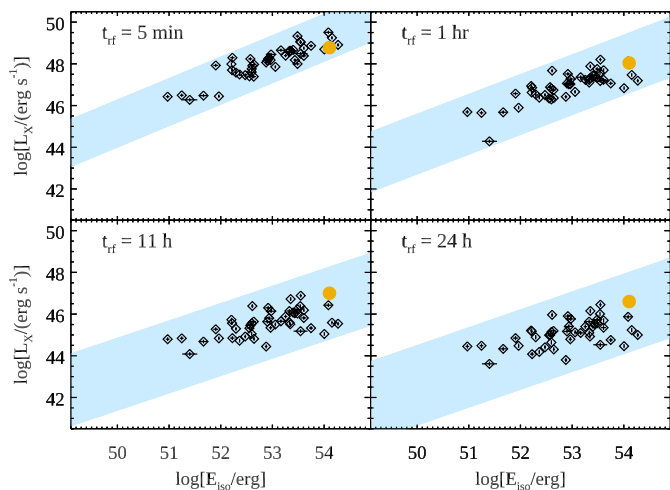


Fig. 11. The $L_X - E_{\text{iso}}$ correlation presented in D’Avanzo et al. (2012) for the long GRBs of the BAT6 sample (diamonds) at different rest-frame times. The shaded area represents the 3σ scatter of the correlations. GRB 210905A is marked with a filled orange circle.

The obtained X-ray light curve was then fitted with a multiply broken power-law, after removing the time intervals showing significant flaring, and then the fits were interpolated or extrapolated to the rest-frame times $t_{rf} = 5 \text{ min}$, $t_{rf} = 1 \text{ hr}$, $t_{rf} = 11 \text{ hr}$, $t_{rf} = 24 \text{ hr}$. As shown in Fig. 11 the properties of GRB 210905A are fully consistent with the $E_{\text{iso}} - L_X$ correlations found for long GRBs by D’Avanzo et al. (2012).

4.9. Long-GRB progenitors at high redshift

At high redshift the Universe is expected to be populated by Pop-III stars, the first stars formed out of gas clouds of pristine composition. Chemical feedback from the supernova explosions of these very massive stars produces metal enrichment within star-forming clouds, raising the metallicity above a critical threshold above which we expect a slow transition of the SFR from massive Pop-III to solar-size Pop-II/I stars (e.g., Schneider et al. 2006; Maio et al. 2010). Determining how this transition takes place is one of the main missing ingredients to understand galaxy formation in the early Universe. All models (e.g., Mészáros & Rees 2010; Toma et al. 2011; Piro et al. 2014) predict Pop-III GRBs to be very energetic events, and with very long intrinsic duration of 10^4 s , making their detection possible even at the highest redshifts. In particular, Toma et al. (2011) suggested that they can release an equivalent isotropic energy up to $\sim 10^{56-57} \text{ erg}$.

In Fig. 12 we compare θ_{jet} and the collimated energy E_γ of GRB 210905A to the KW sample of 43 long GRBs with reliable jet-break time estimates (Tsvetkova et al. 2017, 2021). Considering the uncertainty on the collimation-corrected energy, GRB 210905A lies just outside the 1σ confidence level of the $E_{\text{peak},z} - E_\gamma$ (“Ghirlanda” relation, see Ghirlanda et al. 2004, 2007) and thus well compatible with this relation. The energy values involved in GRB 210905A, both isotropic and collimated, are large but do not significantly differ from those at low redshift (see Figs. 8 and 12). At lower z , other events produce $E \geq 10^{54} \text{ erg}$ isotropically and $E_\gamma \approx 10^{52} \text{ erg}$ collimation-corrected (see also Cenko et al. 2011). The most outstanding example is GRB 130427A at $z = 0.3399$ (see §4.1), the most powerful GRB at $z < 0.9$ (e.g., Maselli et al. 2014; De Pasquale et al. 2016).

The large $E_{p,z}$ and E_γ suggests a large bulk Lorentz factor Γ_0 of the jet. The afterglow light curve, as reported in Fig. 3, decays as a power-law in both the optical and X-ray band from $\lesssim 5000$ s onward (observer frame). This suggests that the afterglow deceleration time happened before this epoch. Following the method in Molinari et al. (2007), an upper limit on this peak time provides a lower limit to the maximum bulk Lorentz factor of the jet²³, namely $\Gamma_0 \gtrsim 200$, assuming a constant density medium $n_0 = 1 \text{ cm}^{-3}$ and the isotropic energy of GRB 210905A (§4.2). With this estimate, and the inferred half-opening angle, the burst is consistent with the $\theta_j \propto \Gamma_0^{-1}$ broad anti-correlation reported in Ghirlanda et al. (2012, see their Fig. 4).

Therefore, GRB 210905A, although extremely bright, is not separated markedly from other classical GRBs at low redshift. As a consequence, based on these simple deductions, it does not suggest a Pop-III origin.

4.10. Star-formation rates at very high redshift

The rate of GRBs can be used to estimate the SFR in the remote Universe (see §1). Recently, Lloyd-Ronning et al. (2019, 2020a,b, and references therein) have argued that at high redshift, the θ_{jet} of GRBs was, on average, narrower than that of closer GRBs (see also Laskar et al. 2014, 2018). This would imply that more stars formed at high redshift than previously estimated. In the left panel of Fig. 12, we report the relation found by the above authors is shown in the $\theta_{\text{jet}} - (1+z)$ plane. GRB 210905A is an outlier event located at $2 - 3\sigma$ from this relation. We observe that the half-opening angle of this GRB at $z = 6.312$ ($\theta_{\text{jet}} \sim 8$ deg) is consistent with the median value of $\theta_{\text{jet}} = 7.4_{-6.6}^{+11}$ deg for GRBs at $z \sim 1$ but larger than the median of $\theta \sim 3.6 \pm 0.7$ deg found using three $z > 6$ bursts (GRBs 050904, 090423, 120521C, Laskar et al. 2014, 2018). When we include GRB 210905A, the median for the $z \gtrsim 6$ bursts is $\theta \sim 6.2 \pm 0.6$ deg, closer to the best value for $z \sim 1$ events. These findings would argue against a putative inverse dependence between z and θ_{jet} .

5. Conclusions

GRB 210905A was a long burst at redshift $z = 6.312$. Our extensive and prompt follow-up observations from optical/NIR to X-ray and gamma-ray bands, starting in the first seconds, has allowed us to study in detail both the prompt and the afterglow phases. We carried out a joint time-resolved analysis of the last of the three pulses of the prompt emission, which is shown to be in agreement with synchrotron emission, similar to other bursts at lower redshifts. Among the sample of ten $z \gtrsim 6$ GRBs known to date, GRB 210905A stands out (together with GRB 050904) for the highest isotropic energy release and afterglow luminosity at late times, but is still consistent with the range of values found for other long GRBs.

The temporal evolution of the afterglow can be interpreted as due to energy injection followed by a decay well in agreement with the slow-cooling scenario and a constant-density (“ISM”) circumburst medium profile within the standard fireball theory. However, the optical and X-ray afterglows are among the most luminous ever detected, in particular in the optical range at $t \gtrsim 0.5$ d in the rest frame, due to its very slow fading and late

jet break. This break at ~ 40 d (observer frame) results in a half-opening angle that is larger than that of other $z > 6$ bursts, thus questioning the putative inverse dependence of the half-opening angle on redshift. The large total energy budget of $E_{\text{total}} > 10^{52}$ erg associated with this GRB likely excludes all but the most extreme magnetar models as a central engine of this GRB. Therefore, our analysis leaves the Kerr black hole as the preferred scenario for the central engine of GRB 210905A. Finally, the shallow evolution before 1 day suggests that the black hole injected energy via stratified mass ejecta with different Lorentz factors.

In summary, this burst is consistent with the “Amati”, “Ghirlanda”, and “Yonetoku” relations. This fact, and the agreement with the $E_{\text{iso}} - L_X$ plane show that GRB 210905A is a very energetic event but still in the upper tail of the prompt energy and X-ray luminosity distributions of long GRBs. It is not unexpected that our view of the high- z GRB Universe is biased towards the most luminous events, simply because our instruments are limited in sensitivity. In other words, despite its outstanding luminosity it is unlikely that the origin of this GRB is different from those of low-redshift GRBs, like a Pop-III progenitor.

GRBs at $z \gtrsim 6$ are rare events from the perspective of today’s follow-up capabilities but are just the tip of the iceberg of a larger population that future proposed missions promise to uncover (e.g., THESEUS, Amati et al. 2018; Gamov Explorer, White et al. 2021) and, in synergy with the largest ground- and space-based telescopes (such as the James Webb Space Telescope, which successfully launched recently), to answer open questions in modern astrophysics such as the identification of the sources responsible for cosmic reionization, and the evolution of SFR and metallicity across the transition from Pop-III stars to Pop-II/I stars.

Acknowledgements. We acknowledge useful discussion with L. Nicastro and A. MacFadyen. A. Rossi acknowledges support from the INAF project Premiale Supporto Arizona & Italia. D.D.F. and A.E.T. acknowledge support from RSF grant 21-12-00250. D.A.K. acknowledges support from Spanish National Research Project RTI2018-098104-J-I00 (GRBPhot). P.D.A., A.M. acknowledges support from PRIN- MIUR 2017 (grant 20179ZF5KS) and from the Italian Space Agency, contract ASI/INAF n. I/004/11/5. D.B.M. acknowledges the European Research Council (ERC) under the European Union’s Seventh Framework Programme (FP7-2007-2013) (Grant agreement No. 725246). - The Cosmic Dawn Center (DAWN) is funded by the Danish National Research Foundation under grant No. 140. K.E.H. acknowledges support by a Postdoctoral Fellowship Grant (217690–051) from The Icelandic Research Fund. C.G.M. acknowledges financial support from Hiroko and Jim Sherwin. Part of the funding for GROND (both hardware as well as personnel) was generously granted from the Leibniz-Prize to Prof. G. Hasinger (DFG grant HA 1850/28-1). This work made use of data supplied by the UK *Swift* Science Data Centre at the University of Leicester.

References

- Amati, L., Frontera, F., Tavani, M., et al. 2002, *A&A*, 390, 81
- Amati, L., O’Brien, P., Götz, D., et al. 2018, *Advances in Space Research*, 62, 191
- Aptekar, R. L., Frederiks, D. D., Golenetskii, S. V., et al. 1995, *Space Sci. Rev.*, 71, 265
- Arnaud, K. A. 1996, in *Astronomical Society of the Pacific Conference Series*, Vol. 101, *Astronomical Data Analysis Software and Systems V*, ed. G. H. Jacoby & J. Barnes, 17
- Band, D., Matteson, J., Ford, L., et al. 1993, *ApJ*, 413, 281
- Barthelmy, S. D., Barbier, L. M., Cummings, J. R., et al. 2005a, *Space Sci. Rev.*, 120, 143
- Barthelmy, S. D., Cannizzo, J. K., Gehrels, N., et al. 2005b, *ApJ*, 635, L133
- Beardmore, A. P., Evans, P. A., Goad, M. R., Osborne, J. P., & Swift-XRT Team. 2021, *GRB Coordinates Network*, 30768, 1
- Becerra, R. L., De Colle, F., Cantó, J., et al. 2021, *ApJ*, 908, 39
- Beniamini, P., Nava, L., Duran, R. B., & Piran, T. 2015, *MNRAS*, 454, 1073
- Beroiz, M., Cabral, J. B., & Sanchez, B. 2020, *Astronomy and Computing*, 32, 100384
- Bertin, E. & Arnouts, S. 2010, *Astrophysics Source Code Library*, ascl

²³ To derive the peak time, we assumed smoothness $k = 1$ and decay indices $\alpha_0 = -0.7$, $\alpha_0 = \alpha_{1,\text{opt}} = 0.69$, before and after the peak, respectively.

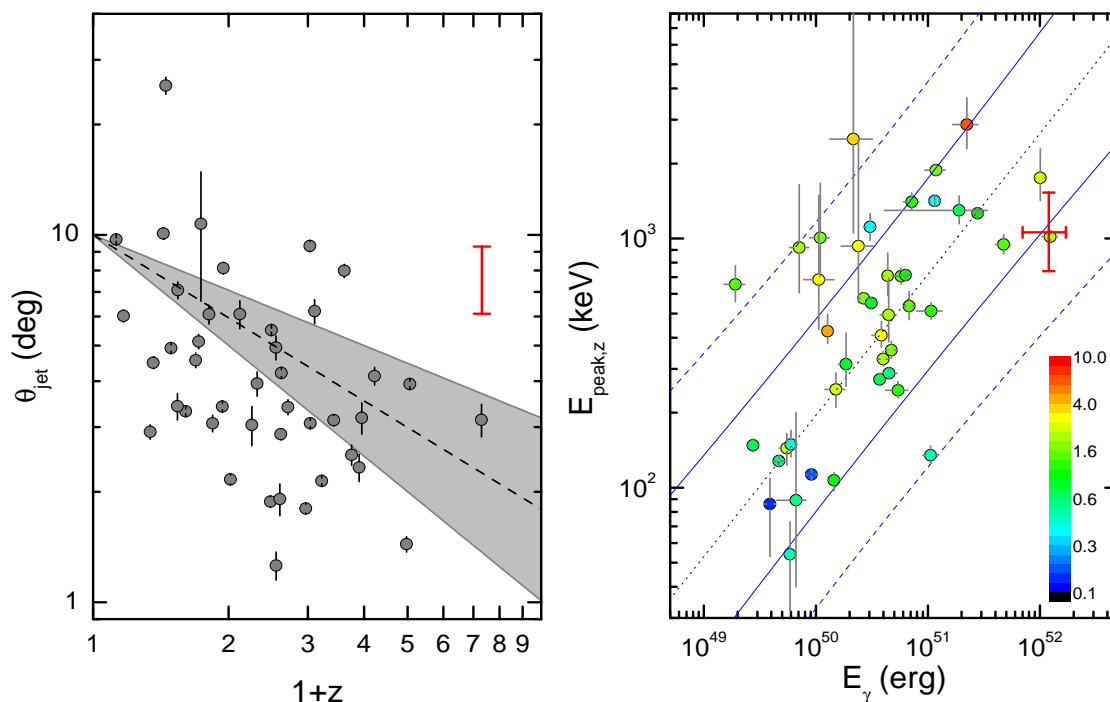


Fig. 12. Collimated parameters of GRB 210905A (red error-bars) compared to a KW sample of 43 long GRBs from Tsvetkova et al. (2017, 2021). We Assumed $\eta = 0.2$ and $n = 1 \text{ cm}^{-3}$ for all bursts. *Left:* Half-opening angle θ_{jet} versus redshift. The dashed line within the grey area show the relation found in Lloyd-Ronning et al. (2020a) with its error.. *Right:* $E_\gamma - E_{peak,z}$ diagram. As in Fig. 8, the color of each data point represents the burst’s redshift. The “Ghirlanda” relation is plotted together with its 68% and 90% PIs.

Beuermann, K., Hessman, F. V., Reinsch, K., et al. 1999, *A&A*, 352, L26
Blain, A. W. & Natarajan, P. 2000, *MNRAS*, 312, L35
Blandford, R. D. & Znajek, R. L. 1977, *MNRAS*, 179, 433
Bloom, J. S., Perley, D. A., Li, W., et al. 2009, *ApJ*, 691, 723
Boër, M., Atteia, J. L., Damerjji, Y., et al. 2006, *ApJ*, 638, L71
Bolmer, J., Greiner, J., Krühler, T., et al. 2018, *A&A*, 609, A62
Bolmer, J., Ledoux, C., Wiseman, P., et al. 2019, *A&A*, 623, A43
Burgess, J. M., Bégué, D., Greiner, J., et al. 2020, *Nature Astronomy*, 4, 174
Campana, S., Salvaterra, R., Ferrara, A., & Pallottini, A. 2015, *A&A*, 575, A43
Castro-Tirado, A. J., Sánchez-Ramírez, R., Ellison, S. L., et al. 2013, arXiv e-prints, arXiv:1312.5631
Cenko, S. B., Frail, D. A., Harrison, F. A., et al. 2011, *ApJ*, 732, 29
Chornock, R., Berger, E., Fox, D. B., et al. 2014, arXiv e-prints, arXiv:1405.7400
Chornock, R., Berger, E., Fox, D. B., et al. 2013, *ApJ*, 774, 26
Corsi, A., Piro, L., Kuulkers, E., et al. 2005, *A&A*, 438, 829
Cucchiara, A., Fumagalli, M., Rafelski, M., et al. 2015, *ApJ*, 804, 51
Cucchiara, A., Levan, A. J., Fox, D. B., et al. 2011, *ApJ*, 736, 7
Dai, Z. G. & Lu, T. 1998, *A&A*, 333, L87
Dall’Osso, S., Stella, L., & Palomba, C. 2018, *MNRAS*, 480, 1353
D’Avanzo, P., Melandri, A., Covino, S., Fugazza, D., & REM Team. 2021, GRB Coordinates Network, 30772, 1
D’Avanzo, P., Salvaterra, R., Sbarufatti, B., et al. 2012, *MNRAS*, 425, 506
De Pasquale, M., Page, M. J., Kann, D. A., et al. 2016, *MNRAS*, 462, 1111
De Pasquale, M., Piro, L., Gendre, B., et al. 2006, *A&A*, 455, 813
Devillard, N. 1997, *The Messenger*, 87, 19
Evans, P. A., Beardmore, A. P., Page, K. L., et al. 2009, *MNRAS*, 397, 1177
Evans, P. A., Beardmore, A. P., Page, K. L., et al. 2007, *A&A*, 469, 379
Evans, P. A., Willingale, R., Osborne, J. P., et al. 2010, *A&A*, 519, A102
Fausley et al. in prep.
Frail, D. A., Kulkarni, S. R., Sari, R., et al. 2001, *ApJ*, 562, L55
Frederiks, D., Golenetskii, S., Lysenko, A., et al. 2021, GRB Coordinates Network, 30780, 1
Freudling, W., Romaniello, M., Bramich, D. M., et al. 2013, *A&A*, 559, A96
Frontera, F., Amati, L., Costa, E., et al. 2000, *ApJS*, 127, 59
Fryer, C. L., Lien, A. Y., Fruchter, A., et al. 2021, arXiv e-prints, arXiv:2112.00643
Fynbo, J. P. U., Starling, R. L. C., Ledoux, C., et al. 2006, *A&A*, 451, L47
Gaia Collaboration, Brown, A. G. A., Vallenari, A., et al. 2018, *A&A*, 616, A1
Galama, T. J., Briggs, M. S., Wijers, R. A. M. J., et al. 1999, *Nature*, 398, 394
Gehrels, N., Barthelmy, S. D., Burrows, D. N., et al. 2008, *ApJ*, 689, 1161
Gehrels, N., Chincarini, G., Giommi, P., et al. 2004, *ApJ*, 611, 1005
Gendre, B., Stratta, G., Atteia, J. L., et al. 2013, *ApJ*, 766, 30
Ghirlanda, G., Ghisellini, G., & Lazzati, D. 2004, *ApJ*, 616, 331

Ghirlanda, G., Nava, L., Ghisellini, G., et al. 2012, *MNRAS*, 420, 483
Ghirlanda, G., Nava, L., Ghisellini, G., & Firmani, C. 2007, *A&A*, 466, 127
Ghisellini, G., Ghirlanda, G., Ogasanoyan, G., et al. 2020, *A&A*, 636, A82
Granot, J. & Sari, R. 2002, *ApJ*, 568, 820
Granot, J. & van der Horst, A. J. 2014, *PASA*, 31, e008
Greiner, J. 2019, *PASP*, 131, 015002
Greiner, J., Bornemann, W., Clemens, C., et al. 2008, *PASP*, 120, 405
Greiner, J., Krühler, T., Fynbo, J. P. U., et al. 2009, *ApJ*, 693, 1610
Greiner, J., Krühler, T., Klose, S., et al. 2011, *A&A*, 526, A30
Grieco, V., Matteucci, F., Meynet, G., et al. 2012, *MNRAS*, 423, 3049
Guetta, D., Spada, M., & Waxman, E. 2001, *ApJ*, 557, 399
Guidorzi, C., Kobayashi, S., Perley, D. A., et al. 2011, *MNRAS*, 417, 2124
Guiriec, S., Kouveliotou, C., Hartmann, D. H., et al. 2016, *ApJ*, 831, L8
Haensel, P., Zdzunik, J. L., Bejger, M., & Lattimer, J. M. 2009, *A&A*, 502, 605
Hartoog, O. E., Malesani, D., Fynbo, J. P. U., et al. 2015, *A&A*, 580, A139
Heintz, K. E., Ledoux, C., Fynbo, J. P. U., et al. 2019, *A&A*, 621, A20
Heintz, K. E., Watson, D., Jakobsson, P., et al. 2018, *MNRAS*, 479, 3456
Hjorth, J., Sollerman, J., Møller, P., et al. 2003, *Nature*, 423, 847
Kann, D. A., Klose, S., & Zeh, A. 2006, *ApJ*, 641, 993
Kann, D. A., Klose, S., Zhang, B., et al. 2011, *ApJ*, 734, 96
Kann, D. A., Klose, S., Zhang, B., et al. 2010, *ApJ*, 720, 1513
Kann, D. A., Masetti, N., & Klose, S. 2007, *AJ*, 133, 1187
Kawai, N., Kosugi, G., Aoki, K., et al. 2006, *Nature*, 440, 184
Kennicutt, Robert C., J. 1998, *ARA&A*, 36, 189
Kerr, R. P. 1963, *Phys. Rev. Lett.*, 11, 237
Kistler, M. D., Yüksel, H., Beacom, J. F., Hopkins, A. M., & Wytthe, J. S. B. 2009, *ApJ*, 705, L104
Kobayashi, S. & Sari, R. 2001, *ApJ*, 551, 934
Kopač, D., Kobayashi, S., Gomboc, A., et al. 2013, *ApJ*, 772, 73
Kouveliotou, C., Meegan, C. A., Fishman, G. J., et al. 1993, *ApJ*, 413, L101
Krühler, T., Küpcü Yıldız, A., Greiner, J., et al. 2008, *ApJ*, 685, 376
Lamb, G. P., Kann, D. A., Fernández, J. J., et al. 2021, *MNRAS*, 506, 4163
Laskar, T., Alexander, K. D., Margutti, R., et al. 2021a, GRB Coordinates Network, 30783, 1
Laskar, T., Berger, E., Chornock, R., et al. 2018, *ApJ*, 858, 65
Laskar, T., Berger, E., Tanvir, N., et al. 2014, *ApJ*, 781, 1
Laskar, T., Margutti, R., Alexander, K. D., Berger, E., & Chornock, R. 2021b, GRB Coordinates Network, 31127, 1
Lattimer, J. M. & Prakash, M. 2016, *Phys. Rep.*, 621, 127
Lipunov, V., Gorbvskoy, E., Kornilov, V., et al. 2021, GRB Coordinates Network, 30766, 1
Lipunov, V., Kornilov, V., Gorbvskoy, E., et al. 2010, *Advances in Astronomy*, 2010, 349171

- Lloyd-Ronning, N., Hurtado, V. U., Aykotalp, A., Johnson, J., & Ceccobello, C. 2020a, *MNRAS*, 494, 4371
- Lloyd-Ronning, N. M., Fryer, C., Miller, J. M., et al. 2019, *MNRAS*, 485, 203
- Lloyd-Ronning, N. M., Johnson, J. L., & Aykotalp, A. 2020b, *MNRAS*, 498, 5041
- Lü, H.-J., Lan, L., Zhang, B., et al. 2018, *ApJ*, 862, 130
- Maio, U., Ciardi, B., Dolag, K., Tornatore, L., & Khochfar, S. 2010, *MNRAS*, 407, 1003
- Maiorano, E., Masetti, N., Palazzi, E., et al. 2005, *A&A*, 438, 821
- Martin-Carrillo, A., Hanlon, L., Topinka, M., et al. 2014, *A&A*, 567, A84
- Maselli, A., Melandri, A., Nava, L., et al. 2014, *Science*, 343, 48
- McCully, C., Volgenau, N. H., Harbeck, D.-R., et al. 2018, in *Software and Cyberinfrastructure for Astronomy v. Vol. 10707*, International Society for Optics and Photonics, 107070K
- McGuire, J. T. W., Tanvir, N. R., Levan, A. J., et al. 2016, *ApJ*, 825, 135
- Melandri, A., Bernardini, M. G., D'Avanzo, P., et al. 2015, *A&A*, 581, A86
- Mészáros, P. & Rees, M. J. 2010, *ApJ*, 715, 967
- Metzger, B. D., Margalit, B., Kasen, D., & Quataert, E. 2015, *MNRAS*, 454, 3311
- Molinari, E., Vergani, S. D., Malesani, D., et al. 2007, *A&A*, 469, L13
- Monet, D. G., Levine, S. E., Canzian, B., et al. 2003, *The Astronomical Journal*, 125, 984
- Nava, L., Ghirlanda, G., Ghisellini, G., & Celotti, A. 2011, *A&A*, 530, A21
- Nicuesa Guelbenzu, A., Klose, S., & Rau, A. 2021, *GRB Coordinates Network*, 30781, 1
- Nousek, J. A., Kouveliotou, C., Grupe, D., et al. 2006, *ApJ*, 642, 389
- Nysewander, M., Fruchter, A. S., & Pe'er, A. 2009, *ApJ*, 701, 824
- Oganesyan, G., Nava, L., Ghirlanda, G., Melandri, A., & Celotti, A. 2019, *A&A*, 628, A59
- Panaitescu, A. 2007, *MNRAS*, 380, 374
- Patel, M., Warren, S. J., Mortlock, D. J., & Fynbo, J. P. U. 2010, *A&A*, 512, L3
- Perley, D. A.,enko, S. B., Corsi, A., et al. 2014, *ApJ*, 781, 37
- Péroux, C. & Howk, J. C. 2020, *ARA&A*, 58, 363
- Pirard, J.-F., Kissler-Patig, M., Moorwood, A., et al. 2004, in *Society of Photo-Optical Instrumentation Engineers (SPIE) Conference Series*, Vol. 5492, *Ground-based Instrumentation for Astronomy*, ed. A. F. M. Moorwood & M. Iye, 1763–1772
- Piro, L., Troja, E., Gendre, B., et al. 2014, *ApJ*, 790, L15
- Planck Collaboration, Ade, P. A. R., Aghanim, N., et al. 2016, *A&A*, 594, A13
- Prasad, V., Sawant, P., Waratkar, G., et al. 2021, *GRB Coordinates Network*, 30782, 1
- Preece, R. D., Briggs, M. S., Mallozzi, R. S., et al. 1998, *ApJ*, 506, L23
- Prochaska, J. X., Dessauges-Zavadsky, M., Ramirez-Ruiz, E., & Chen, H.-W. 2008, *ApJ*, 685, 344
- Racusin, J. L., Karpov, S. V., Sokolowski, M., et al. 2008, *Nature*, 455, 183
- Ravasio, M. E., Ghirlanda, G., Nava, L., & Ghisellini, G. 2019, *A&A*, 625, A60
- Ravasio, M. E., Oganesyan, G., Ghirlanda, G., et al. 2018, *A&A*, 613, A16
- Rees, M. J. & Mészáros, P. 1998, *ApJ*, 496, L1
- Rhoads, J. E. 1997, *ApJ*, 487, L1
- Robertson, B. E. & Ellis, R. S. 2012, *ApJ*, 744, 95
- Ronchi, M., Fumagalli, F., Ravasio, M. E., et al. 2020, *A&A*, 636, A55
- Rossi, A., Schulze, S., Klose, S., et al. 2011, *A&A*, 529, A142
- Saccardi, A., Vergani, S. D., De Cia, A., et al. in prep.
- Salvaterra, R. 2015, *Journal of High Energy Astrophysics*, 7, 35
- Salvaterra, R., Della Valle, M., Campana, S., et al. 2009, *Nature*, 461, 1258
- Salvaterra, R., Ferrara, A., & Dayal, P. 2011, *MNRAS*, 414, 847
- Sari, R. & Piran, T. 1999, *ApJ*, 517, L109
- Sari, R., Piran, T., & Halpern, J. P. 1999, *ApJ*, 519, L17
- Sari, R., Piran, T., & Narayan, R. 1998, *ApJ*, 497, L17
- Schady, P., Savaglio, S., Krühler, T., Greiner, J., & Rau, A. 2011, *A&A*, 525, A113
- Schlafly, E. F. & Finkbeiner, D. P. 2011, *ApJ*, 737, 103
- Schneider, R., Salvaterra, R., Ferrara, A., & Ciardi, B. 2006, *MNRAS*, 369, 825
- Schulze, S., Klose, S., Björnsson, G., et al. 2011, *A&A*, 526, A23
- Schulze, S., Malesani, D., Cucchiara, A., et al. 2014, *A&A*, 566, A102
- Selsing, J., Malesani, D., Goldoni, P., et al. 2019, *A&A*, 623, A92
- Siegel, M. H., Sonbas, E., & Swift/UVOT Team. 2021, *GRB Coordinates Network*, 30785, 1
- Skrutskie, M. F., Cutri, R. M., Stiening, R., et al. 2006, *AJ*, 131, 1163
- Sonbas, E., Ambrosi, E., D'Ai, A., et al. 2021, *GRB Coordinates Network*, 30765, 1
- Stanek, K. Z., Matheson, T., Garnavich, P. M., et al. 2003, *ApJ*, 591, L17
- Starling, R. L. C., Willingale, R., Tanvir, N. R., et al. 2013, *MNRAS*, 431, 3159
- Stratta, G., Dainotti, M. G., Dall'Osso, S., Hernandez, X., & De Cesare, G. 2018, *ApJ*, 869, 155
- Stratta, G., Gendre, B., Atteia, J. L., et al. 2013, *ApJ*, 779, 66
- Strausbaugh, R. & Cucchiara, A. 2021a, *GRB Coordinates Network*, 30770, 1
- Strausbaugh, R. & Cucchiara, A. 2021b, *GRB Coordinates Network*, 30769, 1
- Tagliaferri, G., Antonelli, L. A., Chincarini, G., et al. 2005a, *A&A*, 443, L1
- Tagliaferri, G., Goad, M., Chincarini, G., et al. 2005b, *Nature*, 436, 985
- Tanvir, N., Rossi, A., Xu, D., et al. 2021a, *GRB Coordinates Network*, 30771, 1
- Tanvir, N. R., Fox, D. B., Levan, A. J., et al. 2009, *Nature*, 461, 1254
- Tanvir, N. R., Laskar, T., Levan, A. J., et al. 2018, *ApJ*, 865, 107
- Tanvir, N. R., Le Floc'h, E., Christensen, L., et al. 2021b, *Experimental Astronomy* [arXiv:2104.09532]
- Tanvir, N. R., Levan, A. J., Fruchter, A. S., et al. 2012, *ApJ*, 754, 46
- Thöne, C. C., Kann, D. A., Jóhannesson, G., et al. 2010, *A&A*, 523, A70
- Tody, D. 1993, in *Astronomical Society of the Pacific Conference Series*, Vol. 52, *Astronomical Data Analysis Software and Systems II*, ed. R. J. Hanisch, R. J. V. Brissenden, & J. Barnes, 173
- Toffano, M., Ghirlanda, G., Nava, L., et al. 2021, *A&A*, 652, A123
- Toma, K., Sakamoto, T., & Mészáros, P. 2011, *ApJ*, 731, 127
- Totani, T., Kawai, N., Kosugi, G., et al. 2006, *PASJ*, 58, 485
- Troja, E., Lipunov, V. M., Mundell, C. G., et al. 2017, *Nature*, 547, 425
- Tsvetkova, A., Frederiks, D., Golenetskii, S., et al. 2017, *ApJ*, 850, 161
- Tsvetkova, A., Frederiks, D., Svinkin, D., et al. 2021, *ApJ*, 908, 83
- van Eerten, H. & MacFadyen, A. 2013, *ApJ*, 767, 141
- van Putten, M. H. P. M. & Della Valle, M. 2017, *MNRAS*, 464, 3219
- Veres, P., Roberts, O. J., & Fermi-GBM Team. 2021, *GRB Coordinates Network*, 30779, 1
- Vernet, J., Dekker, H., D'Odorico, S., et al. 2011, *A&A*, 536, A105
- Vestrand, W. T., Wozniak, P. R., Wren, J. A., et al. 2005, *Nature*, 435, 178
- Vestrand, W. T., Wren, J. A., Panaitescu, A., et al. 2014, *Science*, 343, 38
- Virgili, F. J., Mundell, C. G., Pal'shin, V., et al. 2013, *ApJ*, 778, 54
- Wang, X.-G., Zhang, B., Liang, E.-W., et al. 2015, *ApJS*, 219, 9
- Watson, D., Zafar, T., Andersen, A. C., et al. 2013, *ApJ*, 768, 23
- White, N. E., Bauer, F. E., Baumgartner, W., et al. 2021, in *Society of Photo-Optical Instrumentation Engineers (SPIE) Conference Series*, Vol. 11821, 1182109
- Willingale, R., Starling, R. L. C., Beardmore, A. P., Tanvir, N. R., & O'Brien, P. T. 2013, *MNRAS*, 431, 394
- Wolf, C., Onken, C. A., Luvaul, L. C., et al. 2018, *PASA*, 35, e010
- Woodsley, S. E. & Bloom, J. S. 2006, *ARA&A*, 44, 507
- Yonetoku, D., Murakami, T., Nakamura, T., et al. 2004, *ApJ*, 609, 935
- Zafar, T., Møller, P., Watson, D., et al. 2018, *MNRAS*, 480, 108
- Zafar, T., Watson, D., Fynbo, J. P. U., et al. 2011, *A&A*, 532, A143
- Zafar, T., Watson, D. J., Malesani, D., et al. 2010, *A&A*, 515, A94
- Zeh, A., Klose, S., & Kann, D. A. 2006, *ApJ*, 637, 889
- Zerbi, R. M., Chincarini, G., Ghisellini, G., et al. 2001, *Astronomische Nachrichten*, 322, 275
- Zhang, B., Fan, Y. Z., Dyks, J., et al. 2006, *ApJ*, 642, 354
- Zhang, B., Liang, E., Page, K. L., et al. 2007a, *ApJ*, 655, 989
- Zhang, B. & Mészáros, P. 2004, *International Journal of Modern Physics A*, 19, 2385
- Zhang, B. & Yan, H. 2011, *ApJ*, 726, 90
- Zhang, B., Zhang, B.-B., Liang, E.-W., et al. 2007b, *ApJ*, 655, L25
- Zhang, W. & MacFadyen, A. 2009, *ApJ*, 698, 1261
- Zheng, W., Shen, R. F., Sakamoto, T., et al. 2012, *ApJ*, 751, 90

-
- ¹ INAF - Osservatorio di Astrofisica e Scienza dello Spazio, Via Piero Gobetti 93/3, 40129 Bologna, Italy
- ² Ioffe Institute, Politekhnicheskaya 26, St. Petersburg 194021, Russia
- ³ Instituto de Astrofísica de Andalucía (IAA-CSIC), Glorieta de la Astronomía s/n, 18008 Granada, Spain
- ⁴ Università degli Studi di Messina - Dipartimento MIFT, Polo Pappardo, Via F. S. D' Alcontres 31, 98166, Italy
- ⁵ INAF - Osservatorio Astronomico di Brera, Via E. Bianchi 46, I-23807, Merate (LC), Italy
- ⁶ DARK, Niels Bohr Institute, University of Copenhagen, Jagtvej 128, 2200 Copenhagen, Denmark
- ⁷ School of Physics and Astronomy, University of Leicester, University Road, Leicester LE1 7RH, UK
- ⁸ Department of Astrophysics/IMAPP, Radboud University, Nijmegen, Netherlands
- ⁹ Cosmic DAWN Center, Denmark
- ¹⁰ Niels Bohr Institute, University of Copenhagen, Jagtvej 128, DK-2200 Copenhagen, Denmark;
- ¹¹ Thüringer Landessternwarte Tautenburg, Sternwarte 5, 07778 Tautenburg, Germany
- ¹² The Oskar Klein Centre, Physics Department of Physics, Stockholm University, Albanova University Center, SE 106 91 Stockholm, Sweden
- ¹³ University of the Virgin Islands, Number 2 Brewers Bay Rd., St. Thomas, VI 00802, USA
- ¹⁴ College of Marin, 120 Kent Avenue, Kentfield CA 94904
- ¹⁵ INFN - Sezione di Milano-Bicocca, Piazza della Scienza 3, I-20126 Milano, Italy
- ¹⁶ INAF, Osservatorio Astronomico di Capodimonte, Salita Moiariello 16, 80131 Naples, Italy
- ¹⁷ INAF IASF-Milano, Via Alfonso Corti 12, I-20133 Milano, Italy
- ¹⁸ School of Physics and Astronomy, University of Leicester, University Road, Leicester LE1 7RH, UK
- ¹⁹ GEPI, Observatoire de Paris, PSL University, CNRS, 5 Place Jules Janssen, 92190 Meudon, France
- ²⁰ Institut d' Astrophysique de Paris, UMR 7095, CNRS-SU, 98 bis boulevard Arago, 75014, Paris, France
- ²¹ INAF/IASF Palermo, via Ugo La Malfa 153, I-90146 - Palermo, Italy
- ²² Aix Marseille Univ, CNRS, CNES, LAM, Marseille, France
- ²³ Space Science Data Center (SSDC) - Agenzia Spaziale Italiana (ASI), I-00133 Roma, Italy
- ²⁴ INAF - Osservatorio Astronomico di Roma, Via Frascati 33, 00040 Monte Porzio Catone, Italy
- ²⁵ Artemis, Observatoire de la Côte d' Azur, Université Côte d' Azur, CNRS, 06304 Nice, France
- ²⁶ Department of Physics, The George Washington University, 725 21st Street NW, Washington, DC 20052, USA
- ²⁷ Department of Physics and Earth Science, University of Ferrara, via Saragat 1, I-44122, Ferrara, Italy
- ²⁸ INFN Sezione di Ferrara, Via Saragat 1, 44122 Ferrara, Italy
- ²⁹ Centre for Astrophysics and Cosmology, Science Institute, University of Iceland, Dunhagi 5, 107, Reykjavík, Iceland
- ³⁰ Departamento de Ciencias Físicas, Universidad Andrés Bello, Fernández Concha 700, Las Condes, Santiago, Chile
- ³¹ Department of Physics, University of Bath, Claverton Down, Bath, BA2 7AY
- ³² School of Physics and Astronomy and Institute for Gravitational Wave Astronomy, University of Birmingham, Birmingham B15 2TT, UK
- ³³ Mullard Space Science Laboratory, University College London, Holmbury St Mary, Dorking, Surrey, RH5 6NT, UK
- ³⁴ Anton Pannekoek Institute for Astronomy, University of Amsterdam, Science Park 904, 1098 XH Amsterdam, The Netherlands
- ³⁵ Leiden Observatory, University of Leiden, Niels Bohrweg 2, 2333 CA Leiden, The Netherlands
- ³⁶ Max-Planck-Institut für extraterrestrische Physik, Giessenbachstrae 1, 85748 Garching, Germany
- ³⁷ Department of Astronomy and Astrophysics, The Pennsylvania State University, University Park, PA 16802, USA
- ³⁸ Astronomy, Physics, and Statistics Institute of Sciences (APSYS), 725 21st Street NW, Washington, DC 20052, USA
- ³⁹ Physics Department, Lancaster University, Lancaster, LA1 4YB, UK
- ⁴⁰ Key Laboratory of Space Astronomy and Technology, National Astronomical Observatories, Chinese Academy of Sciences, Beijing 100101, China
- ⁴¹ School of Astronomy and Space Sciences, University of Chinese Academy of Sciences, 19A Yuquan Road, Beijing 100049, China
- ⁴² Centre for Astrophysics and Supercomputing, Swinburne University of Technology, Mail Number H29, PO Box 218, 31122 Hawthorn, VIC, Australia
- ⁴³ ARC Centre of Excellence for Gravitational Wave Discovery (Oz-Grav), Hawthorn, 3122, Australia